JᖴM PAPERS

Three-dimensional transition of the flow past an elastically mounted circular cylinder

Rahul Mishra[1,2,3], Rajneesh Bhardwaj[2] and Mark C. Thompson[1],†

[1]Fluids Laboratory for Aeronautical and Industrial Research (FLAIR) Department of Mechanical and Aerospace Engineering, Monash University, Clayton 3800, Australia

[2]Department of Mechanical Engineering, Indian Institute of Technology Bombay, Mumbai 400076, India

[3]IITB-Monash Research Academy, IIT Bombay, Mumbai 400076, India

Floquet stability analysis and direct simulations of a circular cylinder undergoing vortex-induced vibration (VIV) are presented. Simulation predictions are examined for the reduced velocity range over which there is a strong and periodic resonant response: $U_r \in [4.0, 8.0]$, focusing on a mass ratio of $m^* = 2.546$ matching a number of previous investigations. Over most of this range, the dominant wake modes present are analogous to modes A, B and QP (quasi-periodic) observed in a stationary circular cylinder wake. However, at $U_r = 4.5$, the dominant modes are B, QP and a subharmonic mode (SH), whereas at $U_r = 4.0$, the two-dimensional base state switches to a $P + S$ wake. The critical Reynolds number for two- to three-dimensional transition is observed to decrease with an increase of U_r, in line with a decreasing response amplitude. Over this range, the minimum Re for which the wake remains two-dimensional is 202, which occurs at $U_r = 7.5$, but this increases to $Re_{cr} = 300$ at $U_r = 4.5$, noting the critical Reynolds number for a stationary circular cylinder is $Re_{cr} = 189$. The corresponding critical spanwise wavelengths for $U_r = 4.5$ and 8 are $1.4D$ (mode B) and $4.0D$ (mode A), respectively. Simulations indicate that even at $Re = 300$, flow three-dimensionality increases the amplitude of the lower branch considerably. The investigation establishes the role of oscillation amplitude and reduced velocity in three-dimensional transition for elastically mounted systems.

Key words: transition to turbulence, wakes, flow–structure interactions

† Email address for correspondence: mark.thompson@monash.edu

1. Introduction

The fluid–structure interaction problem of vortex-induced vibration (VIV) of a circular cylinder and, in particular, the case where it is elastically mounted and constrained to only oscillate transversely to the free stream, has been well studied in the literature, as can be seen from many comprehensive reviews: Sarpkaya (1979), Bearman (1984), Parkinson (1989), Sarpkaya (2004), Williamson & Govardhan (2004), Williamson & Govardhan (2008), Bearman (2011), Wu, Ge & Hong (2012) and Soti *et al.* (2018), amongst others. Over the last few decades, there have been many two-dimensional (2-D) numerical investigations of VIV at low Reynolds numbers, which, of course, are only valid if the wake remains 2-D. Interestingly, other studies have indicated that the onset of wake three-dimensionality is delayed if the cylinder oscillates transverse to the free stream (Leontini, Thompson & Hourigan 2007; Gioria *et al.* 2009). Since the development of three-dimensional (3-D) flow is likely to strongly affect the VIV response, it is important to understand the Reynolds number limits of the 2-D VIV modelling.

For a stationary cylinder, the transition from a 2-D periodic von Kármán vortex street to a 3-D wake was observed by noticing the discontinuities of the Strouhal number vs Reynolds number curve (Williamson 1988). Two dominant transition modes can be observed in the 3-D wake, which are referred to as mode A and mode B. Stability analysis reveals that the onset of the first 3-D mode, mode A, occurs at $Re_{cr} \approx 190$. Mode A is a spanwise periodic 3-D flow structure with a spanwise wavelength, λ, of approximately four cylinder diameters (D) (Barkley & Henderson 1996). This is consistent with the experimental finding of Williamson (1988), who observed a spanwise wavelength of between $3D$ and $4D$ in the saturated wake beyond transition. A second 3-D wake mode, mode B, predicted to occur at $Re_{cr} = 260$ from Floquet stability analysis (FSA), instead occurs at $Re_{cr} \approx 230$ in experiments because the mode A saturated wake substantially alters the otherwise 2-D base flow. It also has a spanwise periodic structure with a critical wavelength of $\lambda \approx 0.8D$, again consistent with experimental measurements (Williamson 1988).

Stability analysis is concerned with the breaking of flow symmetries as flow parameters (in this case the Reynolds number) are changed. The 2-D Kármán vortex street behind the stationary cylinder possesses spanwise translational and reflectional symmetries. It also possesses a spatiotemporal symmetry, i.e. a half-period time-shift and spatial reflection about the wake centreline result in the same flow state. If the streamwise flow is directed along the x axis and the base flow (U, V) is generated in the (x, y) plane, this symmetry possessed by the 2-D base flow is defined by

$$(U, V)(x, y, t) = (U, -V)(x, -y, t + T/2), \tag{1.1}$$

where T is the base-flow period. Alternatively, expressed in term of spanwise vorticity, Ω, this translates to

$$\Omega(x, y, t) = -\Omega(x, -y, t + T/2). \tag{1.2}$$

Barkley, Tuckerman & Golubitsky (2000) observed that mode A breaks the translational symmetry of the 2-D flow (base flow) $U(x, y, z, t) = U(x, y, z + l, t)$ (where l is an arbitrary real constant), but preserves the spatiotemporal symmetry. Mode B also breaks the translational symmetry, but unlike mode A, mode B also breaks the spatiotemporal symmetry.

Another instability mode, mode C, not found for a stationary cylinder, was (falsely) reported to occur in the wake of square section cylinder (Robichaux, Balachandar & Vanka 1999). However, it does occur for circular cylinder wakes perturbed by tripwires (Sheard,

Thompson & Hourigan 2003). Mode C has an intermediate wavelength and occurs when the 2-D time-dependent wake does not have the exact spatiotemporal symmetry typically seen in the Kármán vortex street of a circular cylinder. In general, mode C appears in a stationary cylinder wake if a symmetry-breaking mechanism is used, such as a tripwire, or, for example, by imposing transverse oscillation. Such a mode is seen in the FSA of a transversely oscillating cylinder (Leontini *et al.* 2007).

Another 3-D mode shown to be theoretically possible in a stationary or oscillating cylinder wake is a quasi-periodic (QP) mode. This mode has a complex-conjugate pair of Floquet multipliers, allowing it to consist of travelling or standing waves (Blackburn & Lopez 2003). Importantly, this means that the perturbation mode and base-flow periods are not commensurate. FSA for a stationary circular cylinder wake shows that mode QP becomes unstable at $Re_{cr} \approx 377$. At this Re, the wake is already highly 3-D in experiments although showing identifiable dominant mode B spanwise structures but displaying spatiotemporal chaos. These unstable 3-D modes have an intermediate spanwise wavelength in the range $1.5D$ to $2D$. In fact, the falsely identified mode C instability observed for a square cylinder wake by Robichaux *et al.* (1999) was actually a QP mode, but with a period that was very close to subharmonic.

The dominant physical mechanisms underlying mode A and mode B instabilities are different. Williamson (1996) suggested that mode A instability was associated with an elliptic instability of the vortex cores, and that mode B instability was associated with an instability of the braid region (which includes the braid shear layer within the near-wake vortex formation region (Leweke & Williamson 1998; Thompson, Leweke & Williamson 2001)). The physical mechanism of mode C appears to be a hybrid of modes A and B (Sheard, Thompson & Hourigan 2005). However, in each of these cases, the instability should perhaps not be identified with a single physical mechanism; for example, there appears to be some evidence that mode B is also influenced by centrifugal instability of near-wake vortices while showing elliptic instability characteristics within the spanwise vortex cores (Ryan, Thompson & Hourigan 2005).

Most of these referenced studies were undertaken for circular cylinders, either fixed or under forced oscillation. They focused on finding the dominant 3-D modes, the influence of Reynolds number, $Re = UD/\nu$, and amplitude of oscillation, $A^* = A/D$, on the observed modes, and the effect of loss of spatiotemporal symmetry of the base flow on mode selection. Here, U is the uniform flow speed, ν is the kinematic viscosity and A the fixed oscillation amplitude.

Typically, for 2-D numerical investigations of VIV, the Reynolds number is chosen to be low enough to ensure a pre-transition 2-D wake. However, potentially interesting VIV wake states can be suppressed if the Reynolds number is too low, and additionally the connection between 2-D modelling and typically higher-Reynolds-number experiments becomes increasingly decoupled. Thus, the question arises as to the Reynolds number limit to ensure the wake is guaranteed to remain 2-D, or alternatively when 3-D modelling must be undertaken. To date, it appears that the FSA of an elastically mounted circular cylinder at low mass ratios has received little attention in the literature. For the forced oscillation case, the variation of amplitude and possible flow state affect the critical Re for different modes (Leontini *et al.* 2007) and hence transition to a 3-D wake. The primary motivation for this study is to determine the Re limits of 2-D VIV simulations, and in particular, whether changes to the standard von Kármán wake state strongly affect wake stability. In effect, by examining free vibration, this study extends the forced-oscillation transition study of Leontini *et al.* (2007) by examining the influence of oscillation frequency, and how deviations from sinusoidal oscillation, deviations from vibration periodicity and

wake–frequency coupling affect wake transition. In this paper, we investigate the critical
Reynolds number for the 2-D to 3-D transition in a VIV system through Floquet analysis
based on high-fidelity numerical simulations. We also undertake some complementary
3-D direct simulations beyond 3-D transition to quantify the effect on the amplitude
response and the wake state. In addition, the effect of mass ratio is considered.

The layout of this paper is as follows. In § 2, the theoretical background of FSA, used
to determine the linear stability of periodic flow, is briefly provided, and the numerical
approach to solve this coupled system is also briefly discussed. The simulation results
are given in § 3 for VIV. In this section, first response curves for a circular cylinder
wake under VIV are presented for $Re = 150, 200$ and 250 to show why 2-D simulations
are inadequate for accurately modelling higher-Re VIV. Next, the instability of Kármán
wake to 3-D perturbations at $Re = 260, 280$ and 300 are discussed, together with the
instability modes. Furthermore, the 3-D transition is investigated in detail for $Re = 300$ as
a function of reduced velocity, including comparing 2-D and 3-D simulation predictions.
3-D predictions at higher Reynolds numbers are also briefly discussed. Finally, the critical
Reynolds number for elastically mounted VIV wakes is presented as a function of reduced
velocity.

2. Methodology

2.1. *Theoretical background*

FSA is used to predict the critical Reynolds number at which a 2-D periodic flow will first
become unstable to 3-D perturbations, similar to how linear stability analysis (LSA) is used
for stationary flows. This approach has been adopted by researchers to establish the onset
of 3-D instabilities for different bluff-body wakes. Barkley & Henderson (1996) examined
a fixed cylinder wake to predict the critical Reynolds number, Re_{cr}, the corresponding
perturbation mode structure and the wavelengths of modes A and B at onset. Previous
instability analyses of other bluff-body wakes include: the square cylinder (Robichaux
et al. 1999), elongated cylinders for different aspect ratios (Ryan *et al.* 2005), toroids
(Sheard *et al.* 2003), transverse-oscillating cylinders (Leontini *et al.* 2007), rotational
oscillating cylinders (Jacono *et al.* 2010) and elliptical cylinders of different aspect ratios
(Leontini, Jacono & Thompson 2015).

For mode A, the Floquet perturbation velocity field ($\boldsymbol{u}' = (u', v', w')$) shows the
following spatiotemporal symmetry (Barkley & Henderson 1996; Robichaux *et al.* 1999):

$$\left.\begin{array}{l} u'(x, y, z, t) = u'(x, -y, z, t + T/2), \\ v'(x, y, z, t) = -v'(x, -y, z, t + T/2), \\ w'(x, y, z, t) = w'(x, -y, z, t + T/2), \end{array}\right\} \tag{2.1}$$

which is the same symmetry present in the 2-D base-flow wake (with $w = 0$). For mode
A, the velocity components, u' and w', have an *even* spatiotemporal symmetry, whereas
the cross-stream velocity v' has an *odd* spatiotemporal symmetry. Combining these, the
representation of the mode by its streamwise vorticity (Ω_x') gives

$$\Omega_x'(x, y, z, t) = -\Omega_x'(x, -y, z, t + T/2), \tag{2.2}$$

which obeys an odd spatiotemporal symmetry.

The velocity components of mode B have a spatiotemporal symmetry that is just the opposite of mode A and can be written as

$$
\left.
\begin{aligned}
u'(x, y, z, t) &= -u'(x, -y, z, t + T/2), \\
v'(x, y, z, t) &= v'(x, -y, z, t + T/2), \\
w'(x, y, z, t) &= -w'(x, -y, z, t + T/2).
\end{aligned}
\right\}
\tag{2.3}
$$

In terms of streamwise vorticity (Ω'_x) this displays an even spatiotemporal symmetry expressed as

$$
\Omega'_x(x, y, z, t) = \Omega'_x(x, -y, z, t + T/2).
\tag{2.4}
$$

The subharmonic mode C has a Floquet multiplier that is real and negative, and shows the following temporal symmetry for the vorticity:

$$
\Omega'_x(x, y, z, t) = \Omega'_x(x, y, z, t + 2T).
\tag{2.5}
$$

Finally, the QP mode, because it is non-commensurate with the base-flow frequency, does not possess such a relationship between flow states at different times.

In terms of flow physics, during shedding, the newly forming braid shear layer lies in close proximity to the previously formed braid. Unlike mode A, for mode B the braid comprises an array of rolled-up streamwise vortex pairs that extend between the spanwise rollers. The disturbances due to the forming braid set the preferred locations and rotation directions of the new braid vortices, giving a specific symmetry that is different from mode A; mode B has an in-phase symmetry for the streamwise vortex pattern.

Blackburn & Lopez (2003) observed the Floquet multiplier for (pure) mode C contained no imaginary component. In addition, the sign of the perturbation field swapped each period, i.e. the 3-D features alternate in sign from one shedding cycle to the next. It leads to a periodic state with a period of oscillation twice that of the fundamental one, i.e. period $= 2T$ (Sheard *et al.* 2005). Superficially, the spatial structure of the mode C perturbation field is similar to that of modes A and B. For a torus, the near-wake of the mode C instability, within approximately three diameters of the ring, bears a strong resemblance to the mode B instability, with strong perturbation vorticity present in the braid region between base-flow vortices. Further downstream, the perturbation field resembles that of the mode A instability, with perturbation vorticity localised within the base-flow spanwise vortex cores.

2.2. *Floquet stability analysis*

As indicated previously, FSA is method to determine the linear stability of the periodic wake to 3-D perturbations. In this analysis, the growth of linear perturbations is evaluated with respect to a pre-calculated periodic base flow. We consider a periodic 2-D wake (base-flow) $U(x, y, t)$ with period T, and analyse its stability with respect to an infinitesimal 3-D perturbation $u'(x, y, z, t)$. The equations that governs the perturbation field are obtained by substituting $U(x, y, t) + u'(x, y, z, t)$ for $u(x, y, z, t)$; $P(x, y, t) + p'(x, y, z, t)$ for p, in (2.11). The governing equations for perturbation growth are obtained
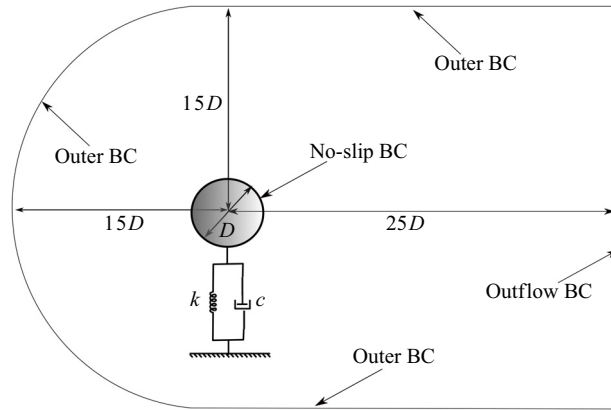
Figure 1. Schematic of the computational domain and the boundary conditions (BC) for Floquet analysis used in the present study.

by linearising to give

$$\frac{\partial \boldsymbol{u}'}{\partial t} = -(\boldsymbol{U} \cdot \boldsymbol{\nabla})\boldsymbol{u}' - (\boldsymbol{u}' \cdot \boldsymbol{\nabla})\boldsymbol{U} - \boldsymbol{\nabla}p' + \frac{1}{Re}(\nabla^2 \boldsymbol{u}'), \tag{2.6}$$

and

$$\boldsymbol{\nabla} \cdot \boldsymbol{u}' = 0. \tag{2.7}$$

These are simplified further by writing the solution as a summation of Fourier terms in the spanwise direction, z. The individual Fourier terms decouple so that the analysis can be done for each Fourier mode (i.e. spanwise wavelength) individually. The detailed approach is described in Barkley & Henderson (1996).

The boundary conditions are shown in figure 1 and are described as follows. The fluid velocity is prescribed at the inlet, top and bottom boundaries, and is given by $(U, V) = U_\infty \mathrm{i} - u_{cyl}\mathrm{j}$. The perturbation velocity components at these far-field boundaries are $u' = v' = w' = 0$, where u', v' and w' are the x, y and z perturbation velocity components, respectively. At the surface of the cylinder, the no-slip condition is imposed, i.e. $(U, V) = 0$ and $(u', v', w') = 0$. At the outlet, the boundary condition is the same as the base-flow condition, i.e. the normal velocity gradient is set to zero for both the base and perturbation velocity fields, and the pressure is fixed. At no-slip boundaries and at the far-field boundaries, higher-order boundary conditions are used for the normal pressure gradient for both the base and perturbation pressure, as described in Karniadakis, Israeli & Orszag (1991).

2.3. *Perturbation kinetic energy*

The transport equation for the perturbation kinetic energy can be derived from the stability equations above by taking the dot product with the perturbation velocity. In tensor notation, which leads to easier manipulation, this gives

$$u_i' \frac{\partial u_i'}{\partial t} = -u_i' U_j \frac{\partial u_i'}{\partial x_j} - u_i' u_j' \frac{\partial U_i}{\partial x_j} - u_i' \frac{\partial p'}{\partial x_i} + \frac{1}{Re} u_i' \frac{\partial}{\partial x_j}\left(\frac{\partial u_i'}{\partial x_j}\right). \tag{2.8}$$

This can be rewritten as

$$\frac{\partial k'}{\partial t} + U_j \frac{\partial k'}{\partial x_j} = -u_i' u_j' \frac{\partial U_i}{\partial x_j} - \frac{\partial u_i' p'}{\partial x_i} + \frac{1}{Re}\left(\frac{\partial^2 k'}{\partial x_j^2}\right), \qquad (2.9)$$

where $k' = \frac{1}{2} u_i' u_i'$ is the perturbation kinetic energy. The left-hand side is just the time derivative of the kinetic energy following an advected fluid parcel whereas the last term represents viscous diffusion of kinetic energy. Of the remaining two terms, the first is the only one referencing the base flow and, hence, represents transfer of energy to and from the base flow, whereas the second represents work done by the perturbation pressure on the perturbation velocity field. Thus, examining the first term on the right-hand side provides insight into the generation of perturbation kinetic energy. Further, by expanding this term into Fourier components in the spanwise direction, i.e. $\boldsymbol{u'} = (\hat{u}(x, y, t)\cos(kz), \hat{v}(x, y, t)\cos(kz), \hat{w}(x, y, t)\sin(kz))$, $p' = \hat{p}\cos(kz)$, and integrating over a spanwise wavelength, gives the spanwise average approximation per unit span as

$$\dot{K}' = \frac{1}{\lambda} \int_0^\lambda \left(-u_i' u_j' \frac{\partial U_i}{\partial x_j}\right) \mathrm{d}z = -\frac{1}{2}\left(\hat{u}\hat{u}\frac{\partial U}{\partial x} + \hat{v}\hat{v}\frac{\partial V}{\partial y} + \hat{u}\hat{v}\left(\frac{\partial U}{\partial y} + \frac{\partial V}{\partial x}\right)\right), \qquad (2.10)$$

where $\lambda = 2\pi/k$ is the wavelength corresponding to wavenumber k. This term can be used to examine which parts of the wake contribute to a particular instability mode.

2.4. *The spectral-element method*

Fluid flow is modelled in the moving reference frame attached to the cylinder so that remeshing is not required. The governing equations are then the non-dimensional Navier–Stokes equations in an accelerated frame of reference (Thompson, Hourigan & Sheridan 1996; Thompson *et al.* 2006)

$$\frac{\partial \boldsymbol{u}}{\partial t} = -(\boldsymbol{u}\cdot\nabla)\boldsymbol{u} - \nabla p + \frac{1}{Re}(\nabla^2 \boldsymbol{u}) - \boldsymbol{a}, \qquad (2.11)$$

and

$$\nabla \cdot \boldsymbol{u} = 0, \qquad (2.12)$$

where $\boldsymbol{u}$ and p are the dimensionless fluid velocity and kinematic pressure, respectively, and $\boldsymbol{a}$ is the acceleration of the reference frame attached to the cylinder, $\boldsymbol{a} = \mathrm{d}\boldsymbol{u}_{cyl}/\mathrm{d}t$, where $\boldsymbol{u}_{cyl}$ is the cylinder velocity vector.

These equations are discretised in space using the spectral-element method (Thompson *et al.* 1996, 2006; Karniadakis & Sherwin 2013). This is essentially a high-order finite-element approach, where the fluid domain is broken up into quadrilateral elements or cells, and within each cell the function is represented by a tensor product of high-order Lagrange polynomial interpolants based on the node points of Gauss–Legendre–Lobatto quadrature. This allows efficient evaluation of the integrals resulting from the application of the weighted residual method to the governing fluid equations. Importantly, the method converges exponentially (or spectrally) as the number of nodes/elements is increased. The method is described in detail in the above references.

In terms of time discretisation, a second-order three-step time-splitting method is used (Karniadakis *et al.* 1991). This treats the effects of advection, mass conservation (and pressure) and diffusion separately. The advection step is treated explicitly using a third-order Adams–Bashforth approximation, whereas the linear pressure and diffusion

substeps are treated implicitly resulting in linear matrix problems. This means that these substeps of the time integration are reduced to matrix–vector multiplies after the computing the lower–upper decomposition of the matrices in a pre-processing step. Further details can be found in Thompson *et al.* (2006). This computational approach is used for both the fluid (2.11), (2.12) and the stability analysis (2.6) equations.

The dimensionless structural differential equation, which provides the acceleration of the cylinder, is given by

$$\ddot{Y}^* + 4\pi\zeta f_n^* + 4\pi^2 f_n^{*2} Y^* = \frac{2}{\pi m^*} C_L. \tag{2.13}$$

Here, $\ddot{Y}^* = \ddot{y}D/U^2$, $\dot{Y}^* = \dot{y}/U$, $Y^* = y/D$ and $C_L = F_y/(\frac{1}{2}\rho_f U^2 DL)$ correspond to the non-dimensional acceleration, velocity, displacement and lift force, respectively, with ρ_f the fluid density and ζ the damping ratio. Here L represents the spanwise length of the cylinder and is taken as 1. In addition, $f_n^* = Df_n/U$ is the non-dimensional natural frequency of the system in a vacuum ($f_n = (1/2\pi)\sqrt{k/m}$), and $m^* = \rho_c/\rho_f$ is mass ratio, with ρ_c the cylinder density. In general, the oscillation response is recorded as a function of the reduced velocity, $U_r = 1/f_n^*$, although often the theoretical system oscillation frequency in the working fluid, which takes account of the added mass contribution, is used to define an alternative reduced velocity instead, i.e. $U^* = 1/f_w^*$, where $f_w^* = Df_w/U$, with $f_w = (1/2\pi)\sqrt{k/(m+m_A)}$. Here, $m_A = C_A\rho_c\pi D^2/4$ is the added mass with $C_A = 1$ for a circular cylinder. There are also two other important frequencies that need to be considered. These are f_v, the shedding frequency of a stationary cylinder, and f or f_y, the actual measured frequency of the cylinder response when the oscillations are periodic. The latter is, of course, different but related to the other frequencies.

These equations are discretised in time following the approach described in Rajamuni, Thompson & Hourigan (2018), and are integrated simultaneously in time with the fluid equations to provide the frame acceleration as a function of time. Typically, we take the damping ratio ζ to be zero.

For the stability analysis undertaken for this study, the fluid (2.11), (2.12) and structural (2.13) equations are integrated in time until a periodic state is reached. At that stage, the velocity field is recorded at discrete integrals (typically 50–100 snapshots) over a complete period. These fields are used to provide the velocity field at each timestep for the linear stability equations (2.6) using quadratic interpolation based on the three closest saved times.

2.5. *Steady to unsteady transition*

The initial Hopf bifurcation (i.e. steady to unsteady transition) for the transition to 2-D periodic flow is also examined for the elastically mounted case. Previously, Mittal & Singh (2005) found that a possible resonance between the shedding and system frequencies could lower the transition Reynolds number considerably from the fixed cylinder case. In this paper, we reexamine this transition especially focusing on the effect of mass ratio.

In terms of stability theory, the transition is from a stationary cylinder to coupled motion, which means we can expand the fluid and body variables about the steady base state as

$$\boldsymbol{u} \rightarrow \boldsymbol{U}(x, y) + \boldsymbol{u}'(x, y, t), \quad p \rightarrow P(x, y) + p'(x, y, t), \quad Y^* \rightarrow Y^{*\prime}(t). \tag{2.14a–c}$$

Thus, after linearising and subtracting the equations of the base flow, the governing stability equations for this case are

$$\frac{\partial \boldsymbol{u}'}{\partial t} = -(\boldsymbol{U} \cdot \nabla)\boldsymbol{u}' - (\boldsymbol{u}' \cdot \nabla)\boldsymbol{U} - \nabla p' + \frac{1}{Re}(\nabla^2 \boldsymbol{u}') - \frac{\mathrm{d}^2 Y^{*\prime}}{\mathrm{d}t^2}, \quad (2.15)$$

$$\nabla \cdot \boldsymbol{u}' = 0, \quad (2.16)$$

together with

$$\ddot{Y}^{*\prime} + 4\pi\zeta f_n^* \dot{Y}^{*\prime} + 4\pi^2 f_n^{*2} Y^{*\prime} = \frac{2}{\pi m^*} C_L'. \quad (2.17)$$

Only the zero damping case is considered here, i.e. $\zeta = 0$.

The dominant eigenmodes can be extracted using the same approach as for the Floquet analysis, i.e. by integrating forward in time from an initial random velocity field until only the most dominant modes remain and then using Arnoldi decomposition on a set of regularly saved snapshots to extract the most dominant modes.

2.6. *3-D simulations*

Subsequent to undertaking the linear and FSA, we also undertook some fully 3-D flow modelling to examine the cylinder response and the wake state post-3-D transition. This was done by extending the 2-D spectral-element code using a Fourier expansion in the spanwise direction as described in Karniadakis & Triantafyllou (1992), Thompson *et al.* (1996) and Gupta *et al.* (2023). Typically, 128 Fourier planes were used to cover a span length of 12D. The latter was chosen as approximately three times the wavelength of mode A. In addition, this gives a spanwise (z) spatial resolution of $\sim 0.1D$, which is much smaller than the smallest instability wavelength (mode B, wavelength $\sim D$). It was also necessary to increase the cross-plane (x–y) resolution for the higher Reynolds number simulations: relative to the 2-D simulations, the intra-element nodal resolution was increased from 8×8 to 10×10 for the $Re = 500$ simulations.

Most simulations at $Re = 1000$ were undertaken by switching on spectral-vanishing viscosity (SVV) in the spectral/spectral-element code (Kirby & Sherwin 2006). This increases the viscosity experienced by shorter length-scale features, which stabilises the code at higher Reynolds numbers. An important point is that the range of length scales (wavelengths) affected decrease as the resolution is increased. Sometimes this is referred to as implicit large-eddy simulation (LES). The implementation and details follow its application and recommended use in the open-source software Nektar++ (described in Kirby & Sherwin 2006), which has been successfully used to simulate flow past a circular cylinder at $Re = 3900$ (Jiang & Cheng 2021), noting an excellent match with PIV velocity fields obtained by Parnaudeau *et al.* (2008) in that case. The implementation of SVV in current code has been verified using the same benchmark $Re = 3900$ non-oscillating cylinder flow, giving statistically identical predictions to the published predictions of Jiang & Cheng (2021).

A resolution study was undertaken to ensure that SVV was minimally influencing statistical maximum response amplitude predictions. Simulations were run for $m^* = 2.456$ using meshes with 518 spectral elements and 128 Fourier planes with both 8×8 and 9×9 noded elements over the entire U^* range. The mode cutoff recommendations provided by Nektar++ documentation, i.e. the lower 75 % of spectral-element (polynomial) modes remained undamped and the SVV diffusion coefficient was set at 0.1 (Nektar++ User Guide, also see Jiang & Cheng (2021) for the $Re = 3900$ cylinder flow predictions and the effect of the choice of SVV parameters). The timestep for these cases was set at

$\Delta t = 0.005 D/U_\infty$. The maximum variation in the amplitude prediction between these two cases across the entire U_r range was less than 2 %, which is consistent with the statistical sampling error given finite integration times. In addition, higher-resolution simulations were undertaken for a reduced velocity corresponding to an upper-branch response ($U^* = 5.0$ or $U_r = 4.2$) using a mesh with 2072 7×7 elements and 128 or 256 Fourier planes. The maximum amplitude response predictions between these four cases were in the range 0.766–0.770, i.e. a variation of approximately 0.5 %. Finally, simulations were undertaken using the 2072 7×7 128 Fourier plane mesh without SVV stabilisation. These were stable for most U^* cases outside the upper branch although a smaller timestep was required for stability. The predicted maximum amplitude responses for the stable simulations were in statistical agreement with the SVV stabilised predictions. In the upper branch, presumably the spatial resolution was not quite adequate to resolve the transfer of energy down to the smallest scales, noting this is a turbulent flow. Although higher resolution could have been used to fully capture scales down to the Kolmorogov scale, this would have been computationally prohibitive, but also noting that this higher-Reynolds-number case is not a major focus of the paper. Of course, the response curve for $Re = 1000$ shown in figure 21 is in good agreement with the predictions of Zhao *et al.* (2014) obtained using a stabilised finite-element code for almost the same mass ratio.

2.7. *2-D resolution studies*

The implementation of the spectral-element approach used in the current study has been validated extensively in previous studies, see, e.g., Hourigan, Thompson & Tan (2001), Sheard *et al.* (2003), Rao *et al.* (2015) and Leontini *et al.* (2007) and references therein. Resolution studies for base flow and stability calculations are considered separately. For the base-flow simulations, the domain and element distribution is based on the previous study of VIV of a circular cylinder, where resolution and other validation studies were reported (Mishra *et al.* 2020). For the stability calculations, care has been taken during the construction of the mesh to ensure adequate resolution, as verified through the base-flow study. However, perturbation fields can have smaller length scales than the base flow, especially as the spanwise wavelength is reduced, so we investigated the convergence with respect to the polynomial order of the tensor-product intra-element interpolating polynomials. Three sets of element resolutions, 6×6, 8×8 and 10×10 (nodes/element) for a parameter set that leads to near-maximal displacement: $Re = 300$, $\zeta = 0.0$, $m^* = 2.546$ and natural frequency $f_n^* = 0.2$ have been used. Figure 2 indicates that increasing the polynomial order from 7 (8×8) to 9 (10×10) changed the value of the Floquet multiplier less than 0.3 % over the range of spanwise wavelengths investigated, providing confidence that the results presented in this paper are adequately converged.

2.8. *Influence of computational domain size*

We also investigated the influence of the locations of the outer computational boundaries relative to the centre of the cylinder. Two different domain sizes were examined. The first domain had dimensions of 15*D* upstream and 25*D* downstream from the cylinder centre, as depicted in figure 1, and was discretised with 518 macro-elements. The second domain extended 50*D* upstream and 50*D* downstream from the cylinder centre, resulting in a mesh consisting of 1134 elements. Figure 3 displays the amplitude of oscillation (A^*) and the root mean square of the lift coefficient ($C_{L,rms}$) for $Re = 150$, $m^* = 2.546$ and $\zeta = 0$. This indicates only minor changes to the response curve over the entire reduced velocity
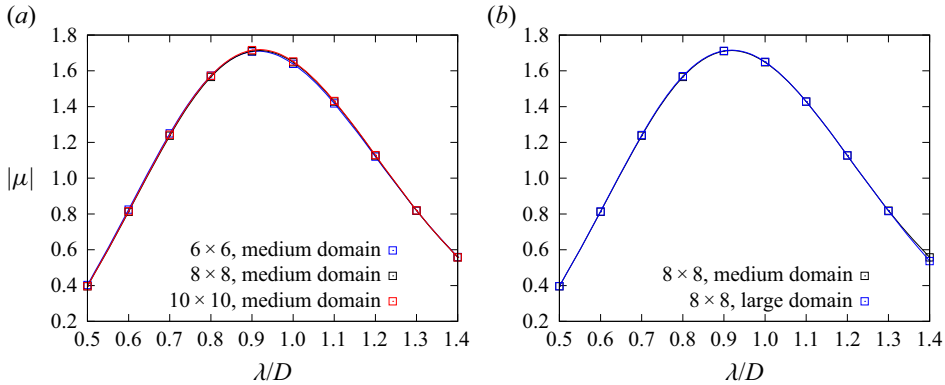
Figure 2. Floquet multiplier modulus, $|\mu|$, vs spanwise wavelength, λ/D, of Floquet modes as a function of number of nodes per spectral element, for a cylinder undergoing VIV at $Re = 300$, $\zeta = 0.0$, $f_n^* = 0.2$ and $m^* = 2.546$: (*a*) influence of element-order on the mode B Floquet multiplier for the mesh used for the bulk of the simulations; (*b*) influence of domain size.
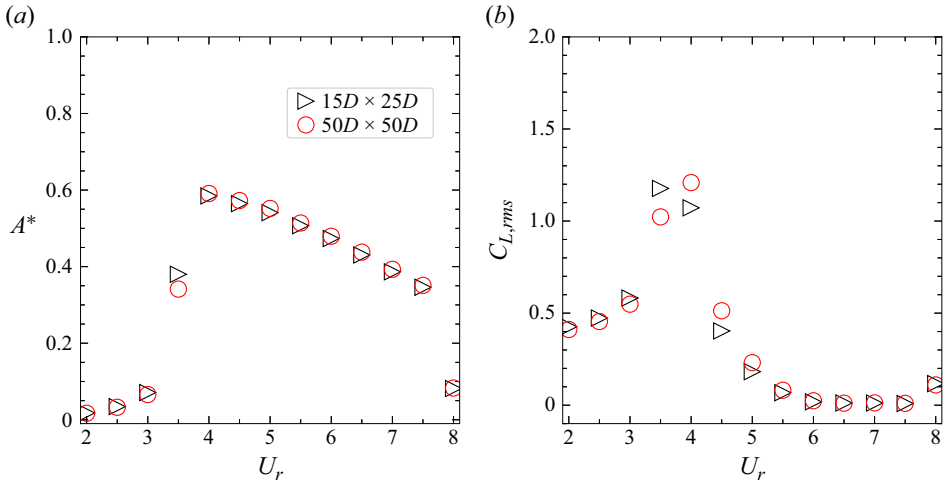

Figure 3. Effect of domain size of amplitude A^* and root mean square of the lift coefficient ($C_{L,rms}$) for $Re = 150$, $m^* = 2.546$ and $\zeta = 0$.

range, with only slightly larger variation in the lift coefficient, which is more sensitive. In addition, the effect on the Floquet multiplier for mode B is shown in figure 2(*b*), which shows a difference of less than 0.2 % near the peak. Thus, the smaller domain size was selected for the remainder of the simulations because of the reduced computational resource requirement for this large parameter study.

2.9. *Validation*

We have undertaken a validation study to ensure that the results produced are in agreement with published results for standard test cases. Comparisons of base-flow VIV predictions for the current set-up against literature results were reported in Mishra *et al.* (2021). We conducted simulations at $Re = 150$ and $m^* = 2.546$ across a range of reduced velocities. Figure 4 illustrates the variations of the maximum displacement of the cylinder, mean lift
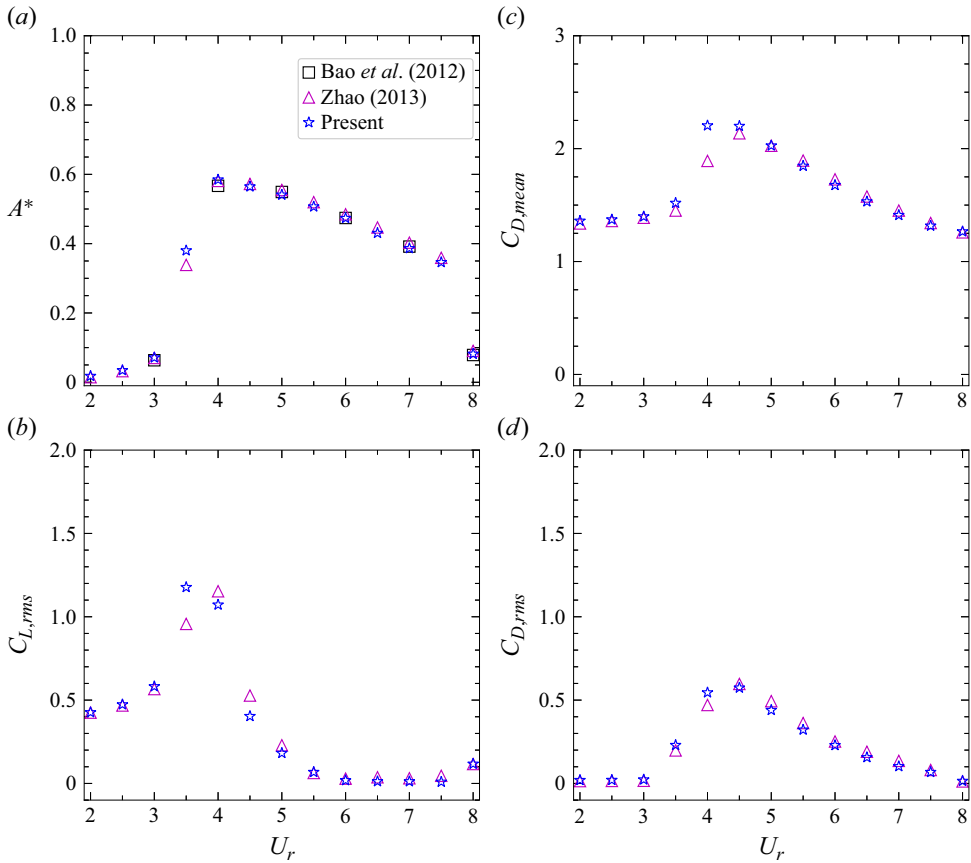
Figure 4. Comparisons of the predicted amplitude response and mean and fluctuating force coefficients against simulation predictions from the literature. Here, $\zeta = 0$, $m^* = 2.546$ and $Re = 150$. See the text for further details.

coefficient and root mean square of drag and lift coefficients with reduced velocity. The comparison reveals that our results closely align with those presented in Bao *et al.* (2012) and Zhao (2013). Any minor differences observed at specific reduced velocities may be attributed to variations in blockage ratios considered.

Validation of stability predictions under VIV is through a comparison against forced oscillation predictions of Leontini *et al.* (2007), while noting that Gioria *et al.* (2009) has produced similar predictions for a different forcing frequency ratio. In particular, Leontini *et al.* (2007) presented a transition map showing where different Floquet modes become unstable as a function of forced oscillation amplitude and Reynolds number for a fixed forcing frequency of $f^* = f(D/U) = 0.2$, noting that this is very close to the vortex shedding frequency at $Re = 200$ and for higher Reynolds numbers after the flow has become 3-D. For the current problem, the oscillation amplitude is a function of the reduced velocity, so by running simulations over a range of Reynolds numbers, the transition Reynolds number can be determined and the oscillation amplitude noted for a particular system frequency. For $f^* = 0.2$, the transition Reynolds number can then be compared with the published result of Leontini *et al.* (2007), under the assumption that the displacement variation is close to sinusoidal in the freely oscillating case.
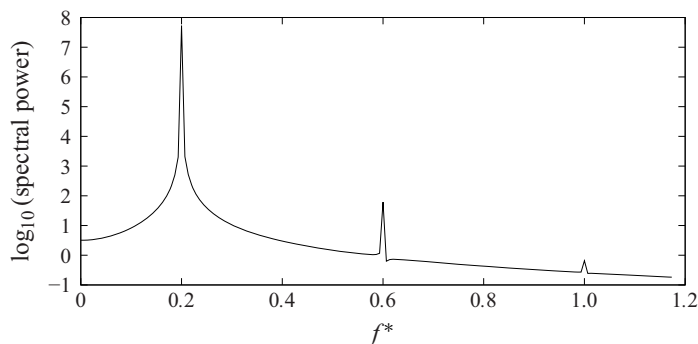
984 A12-12

Figure 5. Power spectrum of the displacement signal for $f^* = 0.2$, $m^* = 2.546$ at $Re = 305$. This indicates that the displacement signal for this reduced velocity ($U_r = 5.194$) the oscillatory response is very close to a pure sinusoid, in accordance with the assumption required for a direct comparison of free and forced vibration cases. See the text for further details.

The validation has been done by extracting the critical Reynolds number corresponding to the observed amplitude for each transition mode from the forced oscillation study of Leontini *et al.* (2007, figure 5). Those predictions show that for an undamped forced oscillation amplitude of $A^* = 0.5$ for $f^* = 0.2$, mode A becomes unstable at $Re_{c,A} \sim 305$ and mode B at $Re_{c,B} \simeq 277$. Thus, simulations were run for $Re = 277$ and 305 for $\zeta = 0$ (undamped system) and $m^* = 2.546$, corresponding to the standard VIV spring–damper system. Since $f_n^* = 0.2$ (i.e. $U_r = 5$) does not give a response oscillation frequency of $f^* = 0.2$, it was first necessary to determine the U_r corresponding to $f^* = 0.2$ for each Reynolds number. For both Reynolds numbers, the saturation amplitude is close to $A \simeq 0.5$. Figure 5 shows the power spectrum of the displacement signal for the $Re = 305$ case, indicating that the response is very close to a pure sine wave with only minor higher-order frequency content at the odd harmonics. Figure 6 shows that at $Re = 277$, the maximum amplitude multiplier is close to unity for the solution branch corresponding to mode B, whereas for $Re = 305$, the maximum amplitude of the mode A branch also reaches a value close to unity. Thus, both of these predictions are in close accord with those from the forced oscillation study, with the same critical Reynolds numbers of $Re_{cr} = 277$ and 305. This provides validation of the implementation of FSA for the elastically mounted spring–damper VIV system. Further validation for the free-oscillation case was provided by examining the initial growth phase of 3-D perturbations for 3-D simulations at post-critical Reynolds numbers, which showed that the measured growth rates in the linear growth regime matched the predictions of FSA. This comparison is not shown because of space considerations.

3. Results

In this section, the stability of the wake to 3-D transition for the VIV for a circular cylinder under elastic support is analysed. There are three independent parameters in this study: mass ratio (m^*), reduced velocity (U_r) and Reynolds number (Re). Recall that the reduced velocity is defined as $U_r = U/(f_n D)$, where U is the free-stream velocity, f_n is the natural frequency of the structure in a vacuum. The limit of two-dimensionality for the oscillating cylinder is determined by varying three independent parameters, Re, U_r, i.e. the non-dimensional oscillation period, and m^*.

We initially analyse an undamped elastically-mounted cylinder for $m^* = 2.546$ at $f_n^* = 0.2$, noting that the natural frequency is close to the natural vortex-shedding frequency of
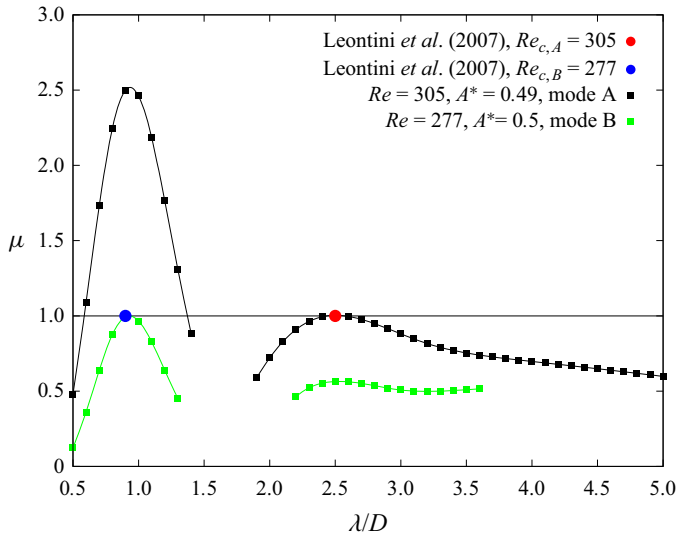
Figure 6. Floquet multiplier vs spanwise wavelength at $Re = 277$ and 305, for $\zeta = 0, f^* = 0.20, m^* = 2.546$, corresponding to a standard spring–damper VIV system. Mode B becomes critical first at $Re \simeq 277$ and then mode A for $Re = 305$. In this figure, A^* is the amplitude of oscillation. A comparison with Leontini *et al.* (2007) shows that for a undamped forced oscillation amplitude of $A^* = 0.5$ and oscillation frequency = 0.2, and for purely sinusoidal oscillation, mode A becomes unstable at $Re_{c,A} \sim 305$ and mode B at $Re_{c,B} \simeq 277$.

a fixed cylinder. The occurrence of modes A, B and QP is examined as Re is increased. We determine the critical values of Re and non-dimensional spanwise wavelength, λ/D, for which the 2-D wake becomes linearly unstable for the periodic oscillation of a cylinder under VIV.

3.1. *Critical Re for the onset of vortex shedding*

Before investigating the loss of stability of the Kármán wake to 3-D perturbations, it is useful to determine the underlying periodic base-flow states. Although this dependence of the transition on reduced velocity has been examined previous by Mittal & Singh (2005) for the two-degree-of-freedom case, they only considered mass ratios $m^* \gtrsim 5$. For the current simulations, this range is extended to lower mass ratios where the effect on transition is amplified.

For a stationary circular cylinder, the wake undergoes a transition from a stable to periodic Kármán wake at $Re \sim 47$ (e.g. Dusek, Gal & Fraunie 1994; Williamson 1996; Le Gal, Nadim & Thompson 2001). This instability leads to unsteady lift and drag forces that cause an elastically mounted cylinder to undergo VIV. The onset of this periodic shedding occurs at different Reynolds numbers for a cylinder undergoing VIV. The value of this critical Re depends on the reduced velocity.

Based on the stability analysis of § 2.5, figure 7 provides growth rate contours for mass ratios $m^* = 1, 2.546$ and 10. The zero growth rate curves are marked, which indicate the transition Reynolds number as a function of reduced velocity.

As U_r is increased from very small values, the critical Reynolds number, Re_{co}, initially rises from a value consistent with the stationary cylinder transition Reynolds number of $Re_{co} \simeq 46$ to reach a peak, prior to rapidly dropping after a different instability mode becomes dominant (corresponding to the system frequency rather than the unsaturated
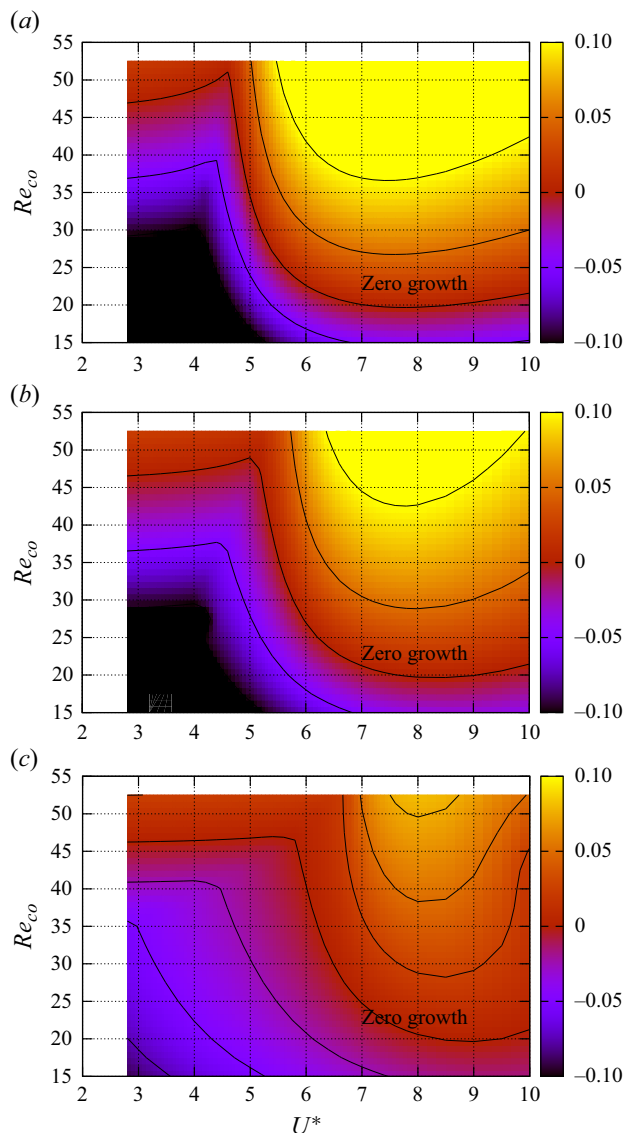
Figure 7. Growth rate contour maps for the steady to unsteady transition of an elastically mounted cylinder showing the effect of mass ratio on transition as a function of reduced velocity. The rows correspond to (*a*) $m^* = 1$, (*b*) $m^* = 2.546$ and (*c*) $m^* = 10$. The zero growth contour is marked indicating the variation of the transition Reynolds number as U^* is varied.

shedding frequency). This shift corresponds to the kinks in the contour lines of figure 7. For the lightest mass ratio considered, $m^* = 1$, the critical Reynolds number is increased to approximately $Re_{co} = 51$ at $U_r = 4.6$. For larger mass ratios, the effect is less; for $m^* = 10$, the increase is only to $Re_{co} \simeq 47$ at $U_r = 5.7$ before again dropping rapidly. In all cases, beyond the initial peak, the critical Reynolds number reaches a value of slightly less than 20, noting that the minimum occurs at different reduced velocities for the different mass ratios. This result is consistent with the findings of Mittal & Singh (2005), who also found a minimum critical Reynolds number of $\sim$20.
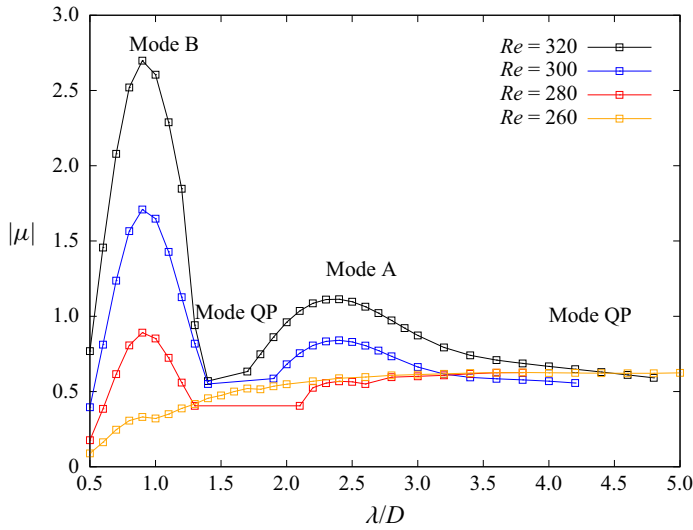
Figure 8. Floquet multiplier vs wavelength at $Re = 320, 300, 280$ and 260; $\zeta = 0$ (undamped system), $f_n^* = 0.20$ and $m^* = 2.546$.

3.2. *Variation of the mode growth close to 3-D transition*

In this section, for the system undergoing VIV, loss of stability of the Kármán wake to 3-D perturbations is analysed for a mass ratio $m^* = 2.546$, as a function of Reynolds number. The Reynolds number range chosen covers the range where analogues of both modes A and B become unstable. Figure 8 shows the magnitude of the predicted Floquet multiplier, $|\mu|$, vs wavelength, λ/D, for undamped free vibration. The natural frequency is fixed at $f_n^* = 0.2$, close to shedding frequency of the fixed cylinder; this corresponds to $U_r = 5.0$. Figure 8 shows that for $Re = 300$ and 320, the flow is unstable to 3-D perturbations, whereas at $Re = 280$ and 260 the 2-D wake flow remains stable ($|\mu| < 1$), with no Floquet modes showing positive growth. The amplitude of oscillation increases slightly with decreasing Re, with $A^* = 0.49, 50, 0.50$ and 0.51, for $Re = 320, 300, 280$ and 260, respectively. The figure shows that for $Re \geq 280$, two clear peaks can be observed although both remain stable at $Re = 280$, whereas for $Re = 260$ only the mode B peak has become visible. The modes corresponding to the two branches are analogous to modes A and B for the stationary cylinder. We observe that mode B becomes critical first then mode A; a similar result was found for $A^* > 0.3$ under forced cylinder oscillation by Leontini *et al.* (2007).

In the case of $Re = 300$, only mode B is unstable, with the maximum growth rate occurring at $\lambda \approx 0.9D$. The multiplier branch corresponding to Mode QP, which has a complex Floquet multiplier, remains stable but is dominant for $1.4D < \lambda < 1.9D$. At $Re = 300$, mode A is also stable with a maximum $|\mu| \approx 0.9$ occurring at $\lambda \approx 2.5D$. In fact, for $\lambda > 3.7D$, the dominant mode has a complex Floquet multiplier corresponding to a QP mode. Since it is observed at a longer wavelength than mode A, to make a clear distinction from the previously observed QP mode, it is designated as mode QPL, named for long-wavelength QP. For $Re = 280$, the flow is near to unstable to mode B, again with a wavelength centred around $\lambda \approx 0.9D$, whereas the branch corresponding to mode QP remains stable and exists for $\lambda > 1.4D$ although it is not shown explicitly here. Thus, modes A and B become critical at lower Reynolds numbers than those of modes QP and QPL. This latter behaviour is similar as that reported by Blackburn, Marques & Lopez

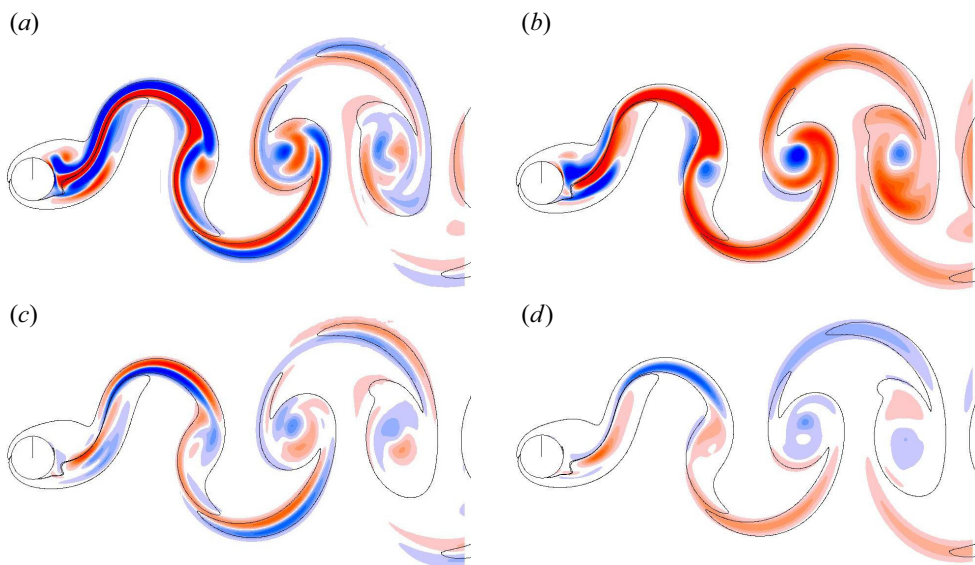**984** A12-16

(*a*)

(*b*)

(*c*)

(*d*)

Figure 9. Spanwise perturbation vorticity depicting (*a,b*) mode B and (*c,d*) mode A at $Re = 300$, $\zeta = 0$, $f_n^* = 0.20$ and $m^* = 2.546$. Red (blue) represents positive (negative) spanwise vorticity. The solid lines outline base-flow vorticity.

(2005) for a stationary cylinder, who estimated the critical *Re* for mode QP to be about 377 with $\lambda_{cr} \approx 1.8D$. Mode QP has no local maximum over this Reynolds number range, unlike modes A and B; however, we have not examined the stability for $Re > 300$.

Figure 9 shows the spanwise and streamwise perturbation vorticity fields at $Re = 300$ in order to indicate the similarities and differences in the structures of modes A and B. The solid lines in the figure outline the base-flow vorticity with two single vortices shed per oscillation cycle (referred to as a 2*S* wake mode). This mode occurs at low amplitudes of oscillation, in particular for $A^* \lesssim 0.5$ at $Re = 300$ (Leontini *et al.* 2006*a*). Mode B in figure 9(*a,b*) is the first occurring unstable mode showing a maximum Floquet multiplier at $\lambda = 0.9D$. Mode B obeys the spatiotemporal symmetry of the base flow about the wake centre line, with spanwise perturbation vorticity repeated (on reflection through the centreline) every half base period. The successive spanwise vortex structures from each side of the wake have the same sign. The still stable mode A correspondingly shows a maximum $|\mu|$ at $\lambda = 2.5D$. This mode is shown in figure 9(*c,d*). The primary vortex at the rear of the cylinder has both positive and negative regions of perturbation vorticity; further downstream, the perturbation becomes concentrated in the primary vortex cores. Mode A has spatiotemporal symmetry opposite to that of mode B. The perturbation field structures for modes A and B are found to be similar to those of modes A and B for a fixed circular cylinder (Barkley & Henderson 1996), although the oscillation certainly has a strong effect on the underlying base flow. In particular, the near-wake base-flow vortex structures are quite different from those for a stationary cylinder in that they are stretched and elongated as the cylinder moves up and down rather than more elliptical in character for the stationary cylinder. Since mode A has been at least partially attributed to elliptic instability (Leweke & Williamson 1998; Thompson *et al.* 2001), this may help to explain why mode A remains stable until higher Reynolds numbers under oscillation. Since mode B is likely to depend more on the shear of the braid regions between Kármán wake vortices (Leweke & Williamson 1998), which of course persist in the oscillatory case,
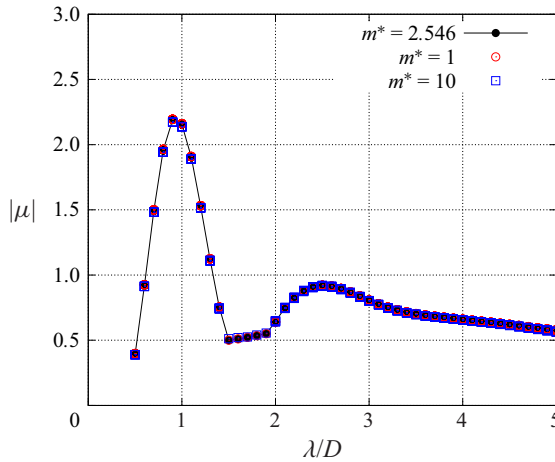
984 A12-17

Figure 10. Floquet multiplier vs wavelength for (*a*) $m^* = 10$, 2.546 and 1, at $Re = 300$ for $f^* = 0.2$.

this is consistent with the smaller effect on the onset of mode B. However, this question is further considered in the following through an examination of the perturbation kinetic energy generation.

The effect of mass ratio on 3-D stability under VIV at $Re = 300$ is examined for mass ratios $m^* = 1$, 2.546 and 10 in figure 10. The reduced velocity is adjusted to result in $f^* = 0.20$ in each case. The response amplitude is close to 0.49 for each mass ratio. Indeed, the dominant Floquet multiplier curves are virtually identical as the mass ratio is varied by a factor of 10, again showing a collapse against the actual system response frequency (rather than U_r or U^*), and consistent with figure 6.

3.3. *Relationship of the 3-D instability modes to stationary cylinder modes A, B and QP*

Figure 11 plots the spatial distributions of the perturbation kinetic energy (k') and generation rate term ($\dot{K}'$) given by (2.10) for the different instability modes. This latter term ($\dot{K}'$) provides the rate of transfer of perturbation kinetic energy to or from the base flow, thus providing insight into which parts of the wake contribute to the development of the instability modes. This analysis was undertaken for modes A, B and QP for the stationary circular cylinder and the analogous A, B and QP instability modes for a cylinder undergoing VIV.
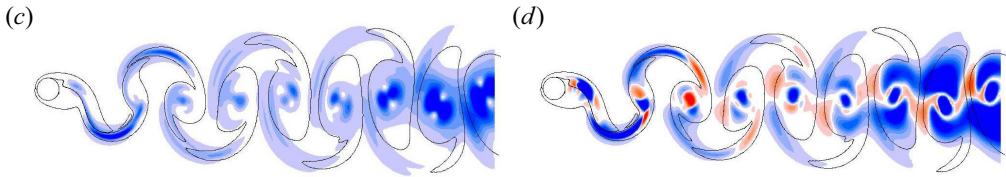
Each pair of rows of this figure shows side-by-side comparisons of the dominant stationary-cylinder and VIV oscillating-cylinder instability modes close to onset. The left column shows perturbation kinetic energy and the right column the perturbation energy generation rate. The top, middle and bottom pair of rows show comparisons for modes A, B and QP, respectively. Clearly, for mode A of the stationary cylinder, energy input into the mode occurs primarily in the wake vortex cores, consistent with the interpretation of elliptic instability assisting the maintenance of the instability (Leweke & Williamson 1998; Thompson *et al.* 2001). On the other hand, for mode B perturbation energy transport from the base flow is primarily in the sheared region between the near-wake vortices and extending into the braids between the row of vortices further downstream. This is consistent with the interpretation that the instability is supported mostly by an instability of the braids (Leweke & Williamson 1998). Mode QP appears to be supported through a more equal combination of elliptic and hyperbolic instabilities (Sheard *et al.* 2003).

984 A12-18

Mode A (Re = 190, λ = 4D), stationary cylinder

(*a*)

(*b*)

Mode A (Re = 305, λ = 2.5D), VIV, U_r = 5

(*c*)

(*d*)
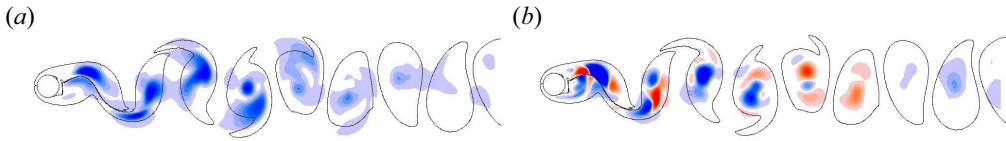
Mode B (Re = 260, λ = 0.9D), stationary cylinder

(*e*)

(*f*)

Mode B (Re = 277, λ = 0.9D), VIV, U_r = 5

(*g*)

(*h*)
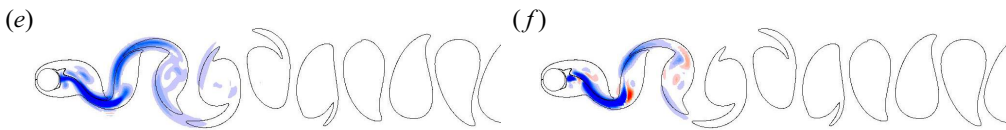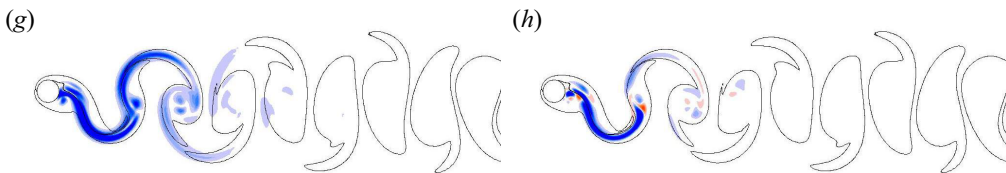
Mode QP (Re = 380, λ = 2D), stationary cylinder

(*i*)

(*j*)

Mode QP (Re = 220, λ = 1.2D), VIV, U_r = 7
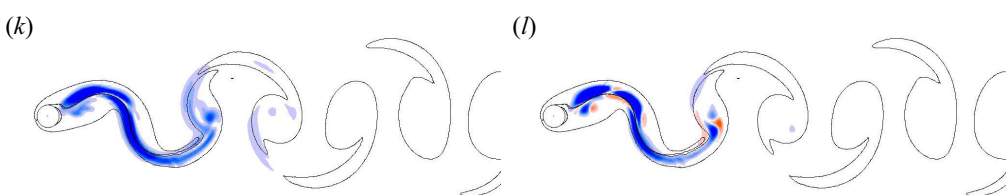
(*k*)

(*l*)
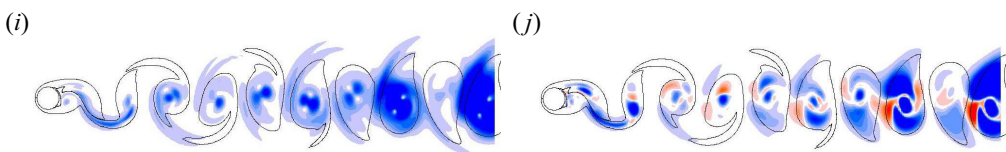
Figure 11. Perturbation kinetic energy, k', (*a,c,e,g,i,k*), and kinetic energy generation rate, $\dot{K}'$, (*b,d,f,h,j,l*), from (2.10), which indicates the generation of perturbation kinetic energy from the base flow: (*a–d*) mode A comparison for the stationary and VIV cases; (*e–h*) same for mode B, bottom two rows; (*i–l*) same for mode QP. See the text for further details.

In terms of the VIV instability modes, mode A shows distinct differences from the k' and $\dot{K}'$ distributions of the stationary cylinder modes. Under oscillation, there appears to be little generation associated with the vortex cores and more generation in the braids. In addition, further downstream, the instability mode appears supported by energy transfer

in the vortex cores, while for the stationary cylinder mode A the generation remains small. The study by Leontini *et al.* (2007) indicates that the mode A seen for a stationary cylinder wake is continuously transformed into the mode A seen under high-amplitude oscillations as the forced oscillation amplitude is steadily increased. Thus, an interpretation of the perturbation kinetic energy analysis is that the stretching of vortex structures in the near-wake caused by the body oscillation suppresses the presence of near-wake elliptic instability, which causes the mode A instability to occur at considerably higher Reynolds numbers ($Re_c \simeq 305$ at $U_r = 5$) than for the stationary case ($Re_c \simeq 190$).

For mode B similar spatial distributions of k' and $\dot{K}'$ are seen for both the stationary and oscillating cylinder modes. Given this, it is not surprising that the instability mode onset is similar in both cases: $Re_c = 259$ for the stationary cylinder and $Re_c = 277$ at $U_r = 5$ for the oscillating cylinder. Thus, mode B is relatively minimally affected by large amplitude oscillations and the non-trivial change to the wake structure, noting a significantly increased wake width.

As shown later in § 3.6, a QP mode is the first occurring VIV instability mode at $U_r = 7$. The comparison of the stationary and VIV QP modes in figure 11 indicates that the VIV QP mode more closely resembles mode B than the stationary cylinder QP mode. Hence, it is unsurprising that the critical Reynolds number for these modes is so different ($Re_c \simeq 377$ for the stationary cylinder mode and $Re_c \simeq 220$ for the VIV mode).

Further discussion on how these modes change with reduced velocity is given in § 3.6.

3.4. *Response curves for a circular cylinder under VIV at Re = 150, 200 and 250*

The VIV response of a circular cylinder for an undamped system is shown in figure 12 at $m^* = 2.546$ for $Re = 150$, 200 and 250. The following variables, the maximum oscillation amplitude (A^*), peak lift coefficient ($C_{L,max}$), normalised frequency (f^*), total phase difference (ϕ_{tot}) and vortex phase difference (ϕ_{vor}), are plotted as a function of reduced velocity (U_r) in figure 12(*a–d*), respectively. Normalised frequency is defined as $f^* = f_y/f_n$, where f_y is the frequency corresponding to the highest power in the power spectral density of displacement, and f_n is the natural frequency of the structural system. The total phase (ϕ_{tot}) and the vortex phase (ϕ_{vor}) are the phase differences between fluid force and displacement signals, obtained using a Hilbert transform (Khalak & Williamson 1999). In particular, ϕ_{tot} and ϕ_{vor} are the mean phase difference between lift force and cylinder displacement, and the vortex force (total − added mass force) and cylinder displacement, respectively.

We observe a typical three-branch response, the initial (red colour), upper (blue colour) and lower (black colour) branches, followed by a desynchronisation (magenta colour) regime. These branches are not necessarily one-to-one related to those observed for high-Reynolds number VIV at a low mass-damping ratio. Based on the observation by Govardhan & Williamson (2000), Leontini, Thompson & Hourigan (2006*b*), Soti *et al.* (2018), Mishra *et al.* (2020) and Sharma, Garg & Bhardwaj (2022), the criteria to classify different VIV branches are as follows. The *initial* branch is demarcated with monotonically increasing A^* and $C_{L,max}$, multiple frequencies in f_y, the vibration frequency overlaps the vortex shedding frequency of a stationary cylinder ($f^* \approx f_v/f_s$), $\phi_{tot} \approx 0$ and $\phi_{vor} \approx 0$. The range of the *upper* branch is identified with large A^*, constant f^* slightly lower than 1 ($f^* < 1$), large $C_{L,max}$, $\phi_{tot} \approx 0$ and transition of ϕ_{vor} from 0 to π. Beyond this, conditions for the existence of the *lower* branch is large A^*, $f^* = 1$, monotonic decrease in $C_{L,max}$, transition of ϕ_{vor} from 0 to π and $\phi_{vor} \approx \pi$. Finally,
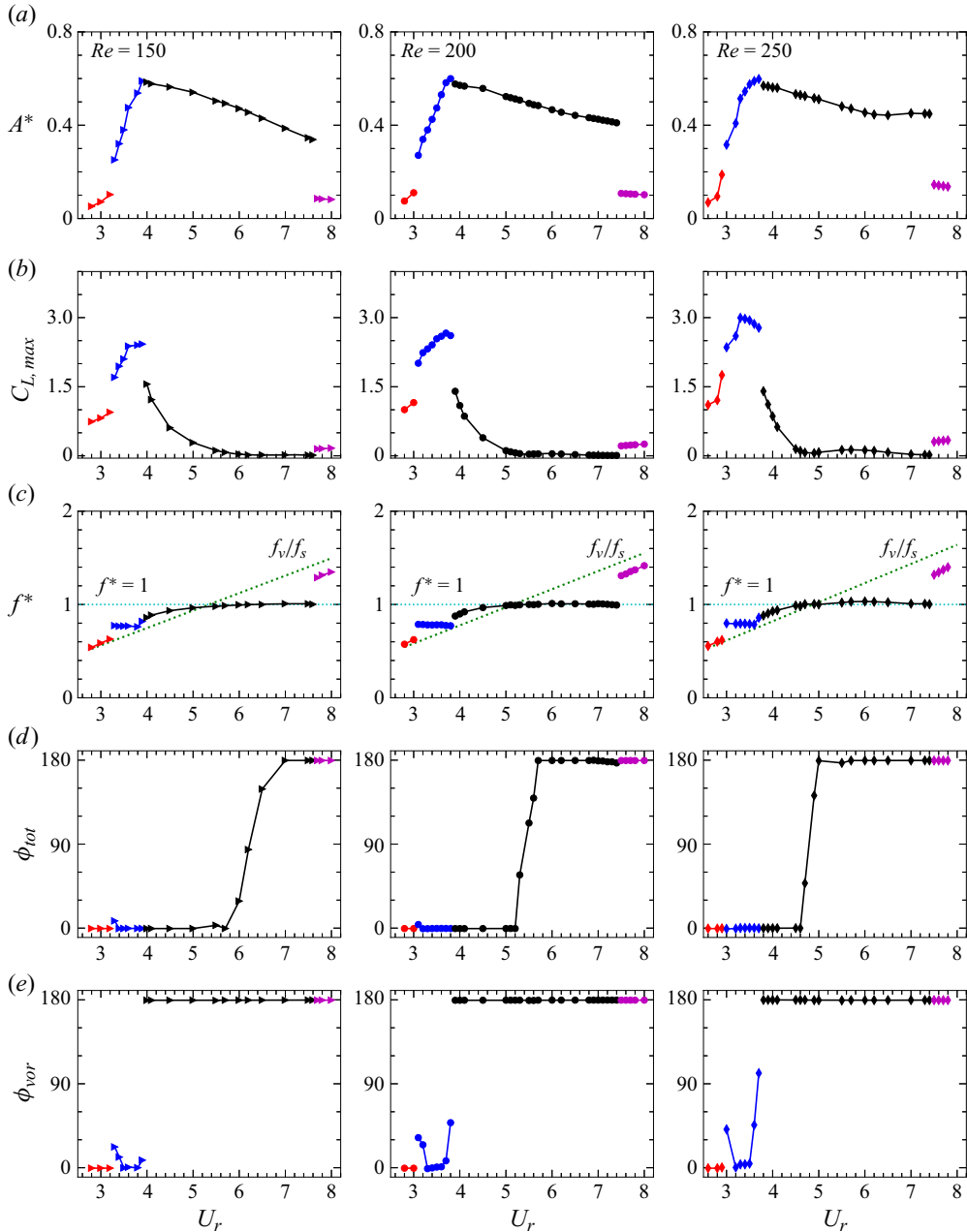
984 A12-20

Figure 12. VIV responses of the cylinder at $m^* = 2.546$ for $Re = 150$, 200 and 250: (*a*) maximum oscillation amplitude, A^*; (*b*) peak lift coefficient, $C_{L,max}$; (*c*) normalised frequency, f^* ($= f/f_n$) (green dotted line represents the vortex shedding frequency for a stationary cylinder); (*d*) mean phase difference between lift force and cylinder displacement, ϕ_{tot}; (*e*) mean phase difference between vortex force and cylinder displacement, ϕ_{vor}.

desynchronisation is characterised by negligible A^*, f^* parallel to f_v/f_s, $\phi_{tot} \approx \pi$ and $\phi_{vor} \approx \pi$.

As evident from figure 12(*a*) A^* is a continuous function of U_r, except there are sudden jumps at $U_r = 3.3$, 3.1 and 3.0 for $Re = 150$, 200 and 250, respectively, thus allowing

984 A12-21

Branch	$Re = 150$	$Re = 200$	$Re = 250$	Demarcating criteria
Initial (red)	[2.8, 3.2]	[2.8, 3.0]	[2.8, 2.9]	A^* and $C_{L,max}$ increases; $f^* = f_v/f_s$; $\phi_{tot} \approx 0$; $\phi_{vor} \approx 0$
Upper (blue)	[3.3, 3.9]	[3.1, 3.8]	[3.0, 3.7]	Large A^*; $C_{L,max}$; $f^* \approx$ constant and $f^* < 1$; $\phi_{tot} \approx 0$; transition of ϕ_{vor} from 0 to π
Lower (black)	[4.0, 7.6]	[3.9, 7.4]	[3.8, 7.4]	Large A^* and monotonically decreasing $C_{L,max}$; $f^* \approx 1$; transition of ϕ_{tot} from 0 to π; $\phi_{vor} \approx \pi$
Desynchronisation (magenta)	[7.7, 8.0]	[7.5, 8.0]	[7.5, 8.0]	Negligible A^*; f^* parallel to f_v/f_s line; $\phi_{tot} \approx \pi$; $\phi_{vor} \approx \pi$

Table 1. Range of U_r and criteria distinguishing the different VIV branches for $Re = 150$, 200 and 250.

the identification of the transition between the initial and the upper branches. Although displacement amplitude is continuous, figure 12(*b*) shows a sudden jump in the lift-force amplitude, thus demarcating the upper and lower branches at $U_r = 4.0$ ($Re = 150$), 3.9 ($Re = 200$) and 3.8 ($Re = 250$). Figure 12(*c*–*e*) shows the branch-to-branch jumps in the oscillation frequency and phase difference. We further quantify the branch ranges for $Re = 150$, 200 and 250 in table 1, together with the criteria used to distinguish the branches.

Figure 12(*a*) shows that the peak oscillation amplitude at all three Reynolds numbers is $\simeq 0.58D$, and the overall response curves are similar for $Re = 150$, 200 and 250. These findings agree with Govardhan & Williamson (2006), who showed that peak oscillation amplitude is almost constant for low-Reynolds-number flows. However, Williamson & Govardhan (2004) has noted that such low-Re simulations, in general, predict peak oscillation amplitudes around $0.6D$, whereas experiments for higher Re produce amplitudes up to $1D$. Figure 13 shows wake vorticity contours at a reduced velocity, $U_r = 4.0$, corresponding to the maximum oscillation amplitude. At $Re = 150$, the wake vortices assemble into a double-row, 2*S* (two single vortices per shedding period), configuration consistent with the high amplitude oscillation (figure 13*a*). At $Re = 200$ and 250 (figure 13*b*,*c*), the newly shed vortices show signs of a 2*P* (two vortex pairs per shedding period) structure close to the rear of the cylinder, although the second vortex of each pair is very weak. However, we certainly do not claim that the wakes have a 2*P* structure for any of these Reynolds numbers, since the experimentally observed 2*P* structures show approximately similar strength opposite-signed vortices in each pair.

On this point, Blackburn, Govardhan & Williamson (2001) compared low Reynolds number experimental results ($Re \sim O(1000)$) with 2-D and 3-D numerical predictions. The 3-D simulations matched the experiments well. Furthermore, demarcation of the upper and the lower branches based on amplitude was not observed for the 2-D simulations, noting that they were clearly evident by the gaps between branches in the 3-D simulation. Therefore, and as has been recognised for a long time, 2-D simulations are inadequate for accurately modelling higher-Re VIV, when the flow is 3-D and turbulent.
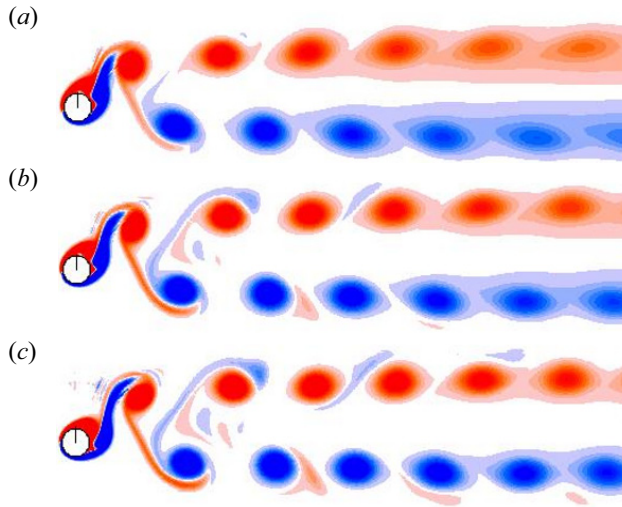
(*a*)

(*b*)

(*c*)

Figure 13. Vorticity contours at $U_r = 4.0$ for Reynolds number (*a*) $Re = 150$, (*b*) $Re = 200$ and (*c*) $Re = 250$. The red (blue) colours represents clockwise (anticlockwise) spanwise vorticity.
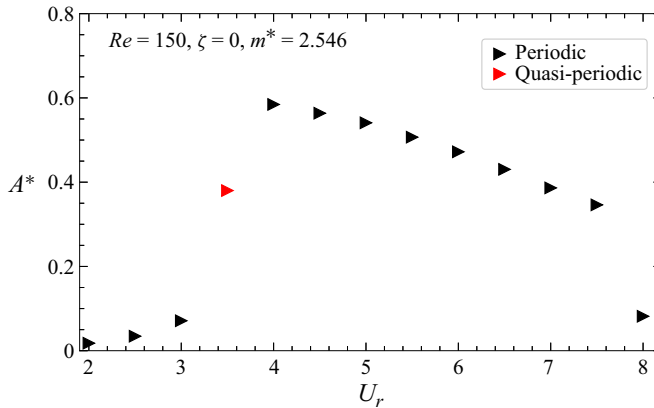

Figure 14. Variation of amplitude (A^*) vs reduced velocity (U_r) for undamped VIV in the range $U_r \in [2.0, 8.0]$, depicting the periodic and QP range.

3.5. *Effect of reduced velocity on different modes*

In § 3.2, stability analysis for VIV is presented for an oscillation frequency of $f_n^* = 0.2$ at $Re = 300$, corresponding to the strongly resonant case. In the current section, results for fixed $Re = 300$ for a standard spring–damper VIV system are presented as a function of reduced velocity. Figure 14 shows the maximum amplitude of vibration vs reduced velocity at $Re = 150$ and for $m^* = 2.546$ depicting the periodic and QP nature of the oscillations. The situation is similar at other Reynolds numbers. Since FSA is only applicable to a periodic base flow, only the reduced velocity range $U_r \in [4.0, 8.0]$ is considered, noting periodic flow together with a strong resonant response.

Figure 15 presents $|\mu|$ as a function of spanwise wavelength for $U_r \in [4.0 - 8.0]$. The $U_r = 4.0$ case has a complex Floquet multiplier corresponding to a stable 2S wake mode, as shown in figure 16. At $U_r = 4.0$ the oscillation amplitude $A^* = 0.56$, corresponds
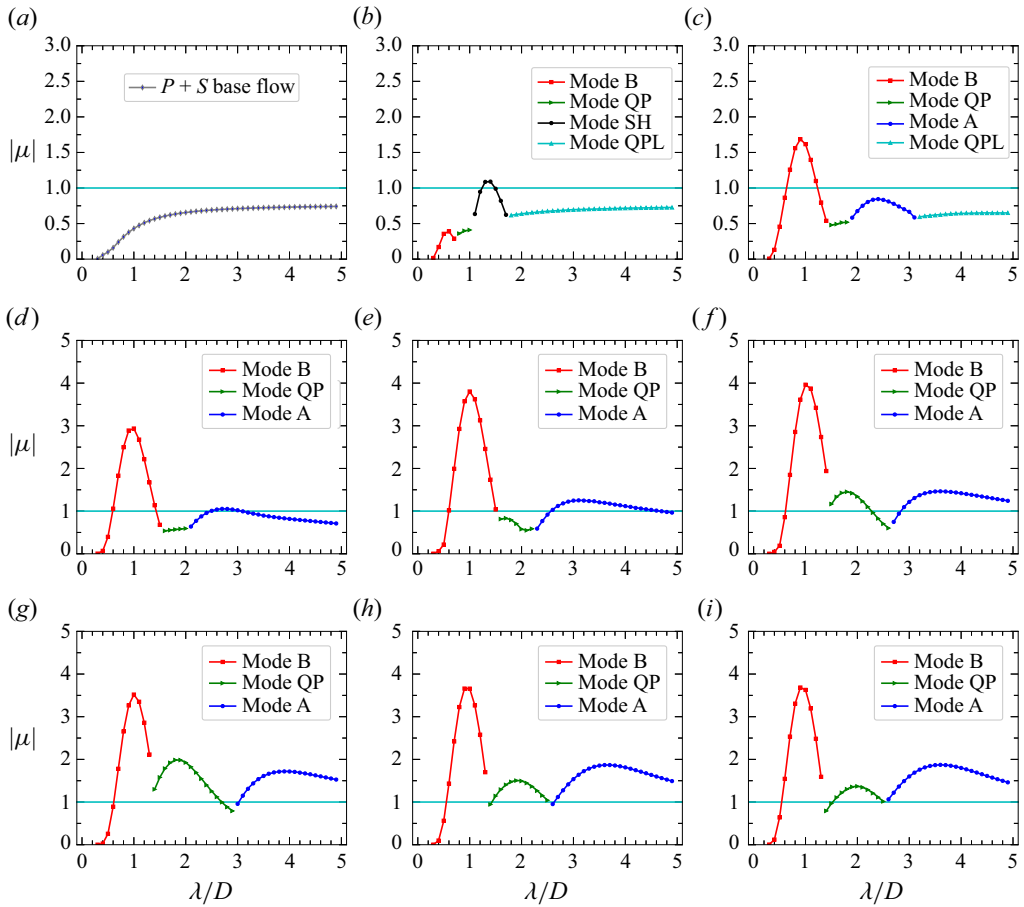
984 A12-23

Figure 15. Floquet multiplier vs wavelength, at $Re = 300$, $m^* = 2.546$, $\zeta = 0$ for: (*a*) $U_r = 4.0$, (*b*) $U_r = 4.5$, (*c*) $U_r = 5.0$, (*d*) $U_r = 5.5$, (*e*) $U_r = 6.0$, (*f*) $U_r = 6.5$, (*g*) $U_r = 7.0$, (*h*) $U_r = 7.5$ and (*i*) $U_r = 8.0$.
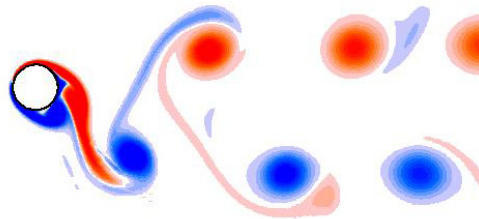

Figure 16. Base-flow vorticity contours at $Re = 300$ for reduced velocity $U_r = 4.0$. The red (blue) represents clockwise (anticlockwise) spanwise vorticity.

to the highest amplitude during VIV. Interestingly, Leontini *et al.* (2007) observed a $P + S$ (base-flow) wake for forced oscillations at $A^* = 0.55$ and $f_s^* = 0.2$. That case corresponds to a forcing frequency of $St = 0.2$ or $U_r \simeq 5.0$. They observed the transition from a $2S$ to $P + S$ wake configuration at $Re = 280$. Thus, the system frequency, which controls the shedding frequency over the resonant range, does have a non-negligible effect on the base-flow structure, with increasing the forcing/shedding frequency leading to a higher-Reynolds-number transition from the $2S$ to the $P + S$ state.
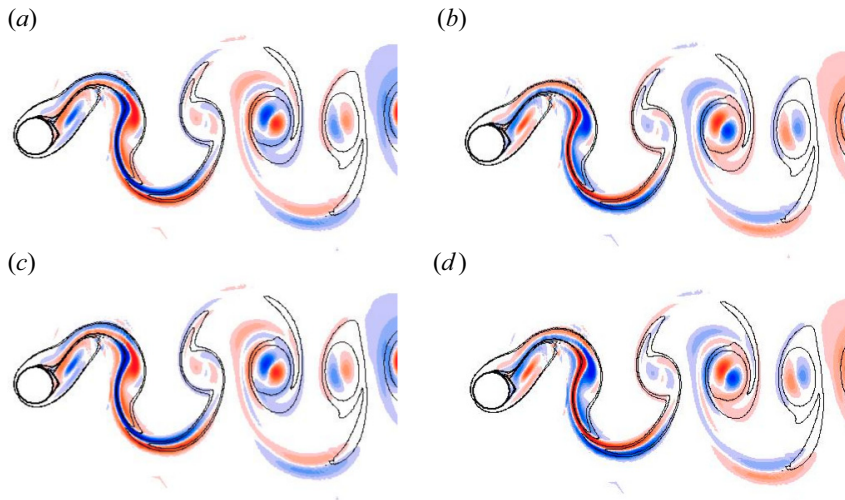
984 A12-24

Figure 17. Spanwise perturbation vorticity indicating mode SH for time (*a*) T, (*b*) $2T$, (*c*) $3T$ and (*d*) $4T$ at $\lambda = 1.4D$, $U_r = 4.5$, $Re = 300$ and $m^* = 2.546$. Here, T is the base-flow field period.

For $U_r \geq 4.5$, modes A, B, QP, QPL (a long-wavelength QP mode) and SH are observed. Of interest, $U_r = 4.5$ shows that a subharmonic mode (SH) is the first to become unstable. This occurs for a wavelength range typically dominated by Mode A. Modes B, QP and QPL are not unstable, whereas mode SH is unstable and grows fastest at $\lambda \approx 1.4D$. Therefore, at $U_r = 4.5$, mode SH is responsible for 3-D transition. It is important to note that the Floquet multiplier for the SH mode is always real and negative consistent with its subharmonic nature. The spanwise perturbation vorticity field is shown in figure 17. The subharmonic mode nature is highlighted by comparing images at each base-flow time period (T), verifying that the perturbation field is repeated over two periods ($2T$) and the structure of the mode is the same at the end of a single period except for a sign change (Sheard *et al.* 2005).

For the $\lambda < 5D$, mode QPL is only observed at reduced velocity $U_r = 4.5$ and 5.0, whereas mode QPL is absent for other reduced velocities $U_r \in [5.5, 8.0]$. It is also observed that as U_r increases, the stability of the modes are affected. For $U_r = 4.0$ the wake is stable, whereas for $U_r = 4.5$ mode SH is just critical and modes B, QP and QPL can be observed. For $U_r = 5.0$, mode A is observed for the first time but remains stable, however mode B is unstable. Furthermore, for $U_r \geq 5.0$, mode B is unstable ($|\mu| > 1$) and $|\mu|$ for this mode increases up to $U_r = 6.5$. The maximum $|\mu| \approx 1.7$ occurs at $\lambda \approx 0.9D$ for $U_r = 5.0$, increasing to a maximum $|\mu| \approx 4.0$ at $\lambda \approx 1.0D$ for $U_r = 6.5$. The growth rate for mode B further decreases at $U_r = 7.0$, with a maximum of $|\mu| \approx 3.5$ at $\lambda \approx 1.0D$, which remains constant on further increasing U_r. The maximum $|\mu| \approx 3.5$ occurs at $\lambda \approx 1.0D$ for $U_r = 7.0$, 7.5 and 8.0.

Similar behaviour can be observed for mode A. At $U_r = 5.5$, the maximum $|\mu| \approx 1.03$ occurs at $\lambda \approx 2.7D$, indicating that the mode is just supercritical. The growth rate increases on further increasing U_r up to $U_r = 7.5$ with a maximum $|\mu| \approx 1.8$ at $\lambda \approx 3.6D$. Beyond $U_r \geq 7.5$, the growth rate remains constant. Mode QP is seen to be stable for $U_r \in [4.0, 6.0]$ and unstable for $U_r \geq 6.0$. The maximum $|\mu|$ increases up to $U_r = 7.0$, with a highest growth rate of $|\mu| \approx 1.9$ at $\lambda \approx 1.9D$. On increasing U_r beyond 7.5, the maximum $|\mu|$ slightly decreases with a maximum of $|\mu| \approx 1.5$ and $|\mu| \approx 1.3$ at $U_r = 7.5$ and 8.0, respectively, centred around $\lambda = 1.9D$. The flow is observed to be more stable at
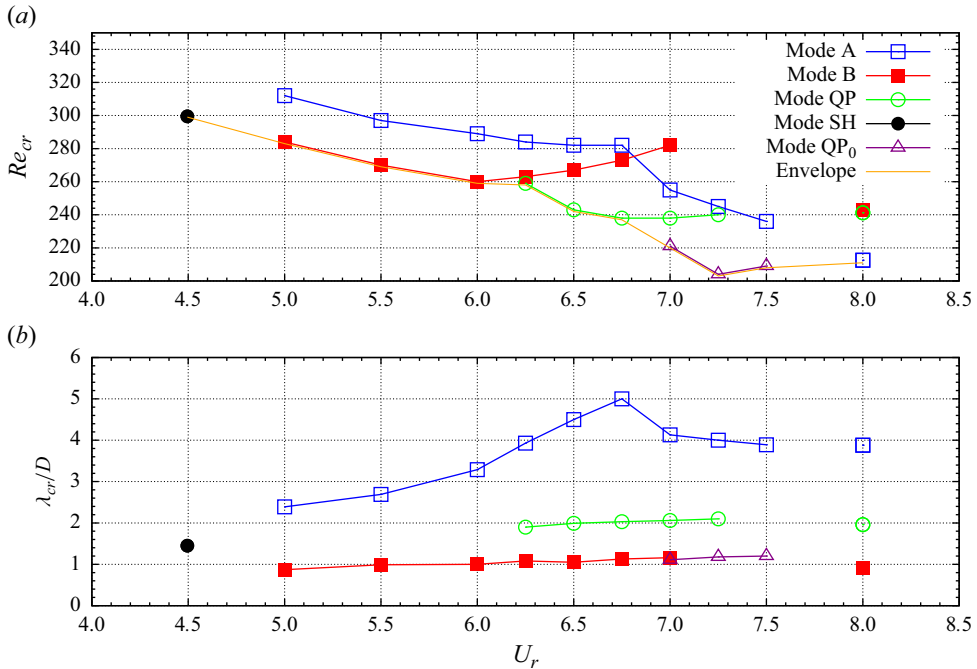
984 A12-25

Figure 18. (*a*) Critical Reynolds number, Re_{cr}, and (*b*) critical wavelength, λ_{cr}, against reduced velocity for the undamped system at $U_r \in [4.5, 8.0]$, and $m^* = 2.546$.

$U_r = 4.0$, 4.5 and 5.0, the highly resonant region. The synchronisation between cylinder vibration and vortex shedding stabilises the flow and hence it is more stable over this range.

3.6. *Critical Reynolds number and wavelength variation with reduced velocity*

This section presents the maximum Re for which the wake remains 2-D for the undamped VIV (standard spring–damper) system as a function of reduced velocity, U_r. We have focused our analysis on the lower branch of VIV, where the base flow exhibits periodic wake oscillations. In the desynchronisation branch, the amplitude is relatively small and periodic with the oscillation frequency close to but lower than the natural shedding frequency. On the other hand, for the initial and (pseudo-)upper branch, the oscillation is not periodic, so FSA, which requires a purely periodic signal, cannot be applied. Thus, we have limited our consideration to the resonant reduced-velocity range, $U_r \in [4.5, 8]$, where the base-flow amplitude variation is periodic, noting that at the upper end of this range corresponds to the desynchonisation branch.

Figure 18 shows the critical Reynolds number, Re_{cr}, and corresponding critical wavelength, λ_{cr}, as a function of reduced velocity, U_r, for an undamped VIV system. Here, Re_{cr} is the value of the Reynolds number at which a given mode first becomes unstable, i.e. μ first exceeds $|\mu| = 1$. In addition, λ_{cr} is the wavelength at which Re_{cr} occurs. To find an accurate Re_{cr} at each U_r, simulations were run for each Re for a series of λ in steps of 0.1. For each Re, μ locally varies quadratically about each local maximum (as shown in previous μ vs λ plots). We determine the coordinate $(|\mu|, \lambda)$ for the local maximum. The value of Re is then incremented in steps of five, noting down the maximum $|\mu|$ and the corresponding value of λ for each Re. This process is repeated until resolving values that give a maximum $|\mu| = 1$. The values of Re_{cr} are then found by interpolating Re and

984 A12-26

corresponding maximum $|\mu|$ values using quadratic interpolation. The same process is repeated for each reduced velocity.

Figure 18 shows the transition boundary for modes A, B, SH and QP, corresponding to reduced velocity [4.5, 8.0]. The critical Reynolds number, Re_{cr}, decreases with reduced velocity up to $U_r = 7.25$. At $U_r = 4.5$, mode SH is the only mode that becomes critical, which occurs at $Re \approx 299$. For $U_r \in [5.0, 6.0]$, modes A and B become critical, with mode B being the leading 3-D mode. At $U_r = 6.25$, mode QP is critical first, with the order of inception of modes being mode QP, mode B and mode A. It is observed that for $U_r = 7.0$ and 7.5, there are two distinct QP modes (referred to as QP and QP_0) together with mode A that become critical, with mode QP_0 becoming critical first. Interestingly, mode QP_0 does not become critical at $U_r = 6.25$. The perturbation kinetic energy analysis (see figure 11 and the discussion in § 3.3) suggests that the physical triggering mechanism for this mode has more in common with mode B rather than mode QP. It also occurs for the same wavelength band as for mode B, however, the transition Reynolds number is much lower than observed for mode B. Also for this U_r range, at $U_r = 7.25$ and $Re > 270$, the wake develops asymmetry about the centreline and the wake period doubles. This part of parameter space is where the transition to mode B would be expected to occur. Transition to the desynchronisation branch occurs between $U_r = 7.5$ and 8.0, resulting in the relatively sudden shifting of shedding and cylinder oscillation to the be close to the natural shedding frequency, and a significant decrease in oscillation amplitude. At $U_r = 8.0$, mode A precedes the occurrence of modes B and QP, with modes B and QP transitioning at approximately the same Re. Interestingly, the transition Reynolds numbers and wavelengths of modes A and QP at $U_r = 8.0$ are consistent with the trends at lower U_r values, despite the significant change in oscillation frequency and amplitude. Mode B, on the other hand, shows a significantly lower transition Reynolds number for this case.

The transition boundary, corresponding wavelength and amplitude for modes A, B, QP and SH, and for $U_r \in [4.5, 8.0]$, are summarised in table 2. These findings are in accordance with Leontini *et al.* (2007) for the forced oscillation case: for $A^* < 0.3$ mode inception order (with increasing Re) is A, B and QP; whereas for $0.3 < A^* < 0.55$, the order of mode inception is B then A; and for $A^* > 0.55$ mode SH is the only unstable mode. Table 2 indicates that for $U_r \in [4.5, 7.5]$, A^* decreases approximately from 0.52 to 0.42 with U_r, whereas for $U_r = 8.0$, $A^* \approx 0.11$. Mode SH occurs at $A^* \approx 0.52$ for $U_r = 4.5$, slightly varying from the prediction of Leontini *et al.* (2007), who observed mode SH at $A^* > 0.55$. For $U_r \in [5.0, 6.0]$ with $0.42 \leq A^* \leq 0.50$ results are in agreement with Leontini *et al.* (2007). It is also observed that for $U_r = 6.5$ and 7.5, $0.40 \leq A^* \leq 0.44$, mode QP first becomes critical, which is different from Leontini *et al.* (2007); however, of course, the system frequency is then significantly different from the forcing frequency of $St = 0.2$ used in that study. On the other hand, at $U_r = 8.0$ with $A^* \simeq 0.11$ and the shedding frequency is close to 0.2, modes A and B undergo transition at close to the values seen for the forced oscillation case: $Re_{cr} = 243$ at $St = 0.18$ (VIV) compared with $Re_{cr} = 255$ at $St = 0.20$ (forced) for mode B; and $Re_{cr} = 212$ at $St = 0.18$ (VIV) compared with $Re_{cr} = 230$ at $St = 0.20$ (forced) for mode A. Overall, there appear to be non-negligible effects of the oscillation frequency and amplitude on transition.

The envelope of the transition lines in figure 18(*a*) shows the variation of critical Reynolds number with reduced velocity for which the flows remains 2-D. The critical Reynolds number decreases with reduced velocity over the entire range of U_r considered. Specifically, $Re_{cr} \approx 299$ at $U_r = 4.5$, decreasing monotonically to $Re_{cr} \approx 208$ at $U_r = 7.5$.

Reduced velocity	Mode A	Mode B	Mode SH	Mode QP	$f(D/U)$
$U_r = 4.5$	—	—	$Re = 299.3$ $\lambda = 1.4$ $A^* = 0.52$	—	0.2234
$U_r = 5.0$	$Re = 311.8$ $\lambda = 2.4$ $A^* = 0.49$	$Re = 283.5$ $\lambda = 0.9$ $A^* = 0.50$	—	—	0.2043
$U_r = 5.5$	$Re = 296.8$ $\lambda = 2.7$ $A^* = 0.47$	$Re = 270.2$ $\lambda = 1.0$ $A^* = 0.48$	—	—	0.1878
$U_r = 6.0$	$Re = 289.2$ $\lambda = 3.3$ $A^* = 0.43$	$Re = 261.3$ $\lambda = 1.0$ $A^* = 0.45$	—	—	0.1729
$U_r = 6.5$	$Re = 282.1$ $\lambda = 4.3$ $A^* = 0.40$	$Re = 267.5$ $\lambda = 1.1$ $A^* = 0.43$	—	$Re = 243.6$ $\lambda = 2.0$ $A^* = 0.45$	0.1567
$U_r = 7.0$	$Re = 256.5$ $\lambda = 4.1$ $A^* = 0.45$	—	—	$Re = 220.6$ $\lambda = 1.1$ $A^* = 0.44$	0.1434
$U_r = 7.5$	$Re = 236.5$ $\lambda = 3.9$ $A^* = 0.44$	—	—	$Re = 208.7$ $\lambda = 1.2$ $A^* = 0.42$	0.1750
$U_r = 8.0$	$Re = 212.4$ $\lambda = 3.9$ $A^* = 0.11$	$Re = 242.5$ $\lambda = 0.9$ $A^* = 0.13$	—	$Re = 241.9$ $\lambda = 2.0$ $A^* = 0.13$	0.1781

Table 2. Transition boundary characteristics: corresponding critical Reynolds numbers, wavelengths and amplitudes for modes A, B, SH and QP. The post-simulation oscillation frequency is shown in the last column corresponding to the Reynolds number of the first transition.

Figure 18(*b*) shows the variation of λ_{cr} with reduced velocity. In terms of the first modes to become unstable, the figure shows that $\lambda_{cr} \approx 1.4D$ for mode SH at $U_r = 4.5$. For $U_r = 5.0$ to 6.5, $\lambda_{cr} \approx 0.9D$ for mode B, however, for mode A there is an increase in λ_{cr} from $2.4D$ to $4.3D$. On further increasing U_r, λ_{cr} for mode A decreases towards $3.9D$ at $U_r = 8.0$. Mode QP, which appears for $U_r \geq 6.5$, decreases from $\lambda_{cr} \approx 2.0D$ to $\lambda_{cr} \approx 1.0D$ over the interval $6.5 \leq U_r \leq 7.5$. It then increases to $\lambda_{cr} \approx 2.0D$ at $U_r = 8.0$. The critical values for $U_r = 8.0$, where the oscillation amplitude is only 0.11, are close to those for the non-vibrating case (Barkley & Henderson 1996) as should be expected.

Overall, the synchronisation between cylinder vibration and vortex shedding has a significant role in maintaining the two-dimensionality of the flow. Clearly, high-amplitude oscillations delay onset of 3-D transition but there is also a distinct dependence on reduced velocity. In summary, for the standard elastically mounted VIV system, the maximum Re for which the wake remains 2-D over the resonant and periodic reduced-velocity range $U_r \in [4, 8]$ is 208 and occurs at $U_r = 7.5$, corresponding to a critical wavelength of $\lambda_{cr} \approx 1.2D$. The maximum delay in the transition from 2-D to 3-D flow occurs for $U_r = 4.5$, with the wake remaining 2-D up to $Re_{cr} \approx 299$.

3.7. *Influence of mass ratio on the amplitude response and transition*

Figure 19 shows the influence of mass ratio on the amplitude response under VIV as a function of Reynolds number. The subfigures in the first column correspond to (*a*) $Re = 150$ (where the wake is certainly 2-D), (*b*) $Re = 200$ (with the wake on the
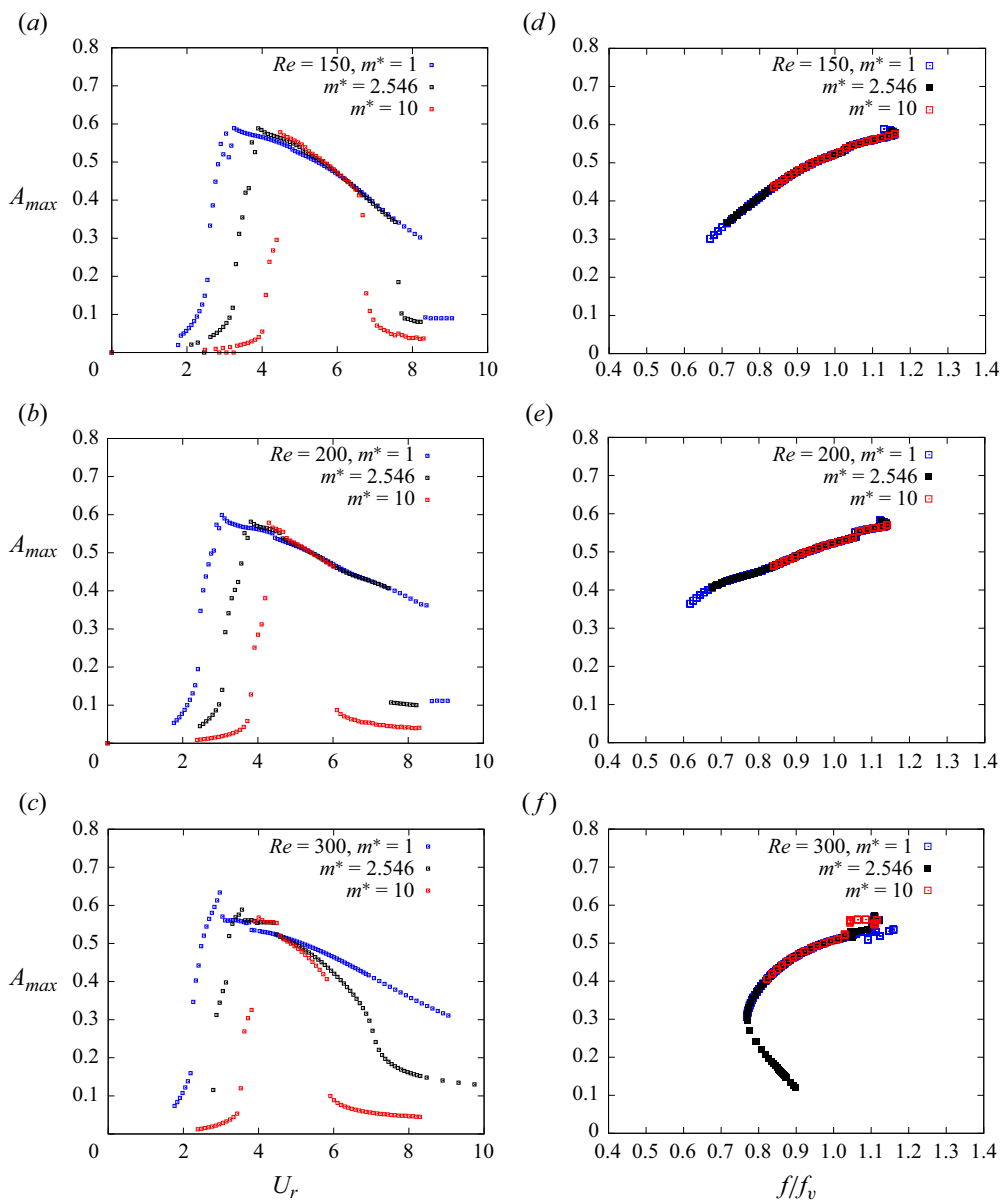
Figure 19. (*a*–*c*) Amplitude response for different Reynolds numbers and mass ratios. (*d*–*f*) Corresponding amplitude response against f/f_v for the same cases in the left column.

verge of transition) and (*c*) $Re = 300$ (where the wake is mostly 3-D). The response curves have a similar shape but with the onset reduced velocity of resonance shifted to the right as the mass ratio is increased. In addition, desynchronisation occurs at smaller U_r values for higher mass ratios. The right-hand column provides the equivalent amplitude curves but plotting against the ratio of actual system oscillation frequency (and vortex shedding frequency under VIV) to vortex shedding frequency for a stationary cylinder. The displacement response is only plotted for the resonant U_r range where the oscillation is periodic. Clearly, for each Reynolds number, there is an excellent collapse of the
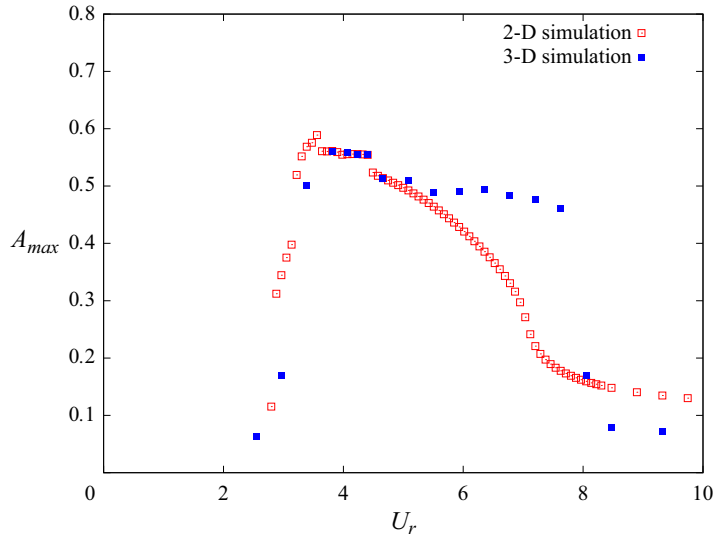
Figure 20. Amplitude response for 2-D and 3-D simulations with respect to U_r at $Re = 300$ for $m^* = 2.546$.

amplitude response for the wide range of mass ratios considered. As already commented, higher mass ratios result in the resonance dropping out at higher oscillation amplitudes as U_r is increased; however, the shape of the curves remains the same. The only slight variation where this does not occur is in the neighbourhood of the maximum amplitude response for $Re = 300$, where there are differences in the maximum response amplitude for the different mass ratios. The upshot of this collapse suggests that the transition scenario discussed in the previous section should hold for other mass ratios by using the post-simulation measured oscillation frequency as the scaling parameter rather than U_r. To this end, table 2 also provides the oscillation frequency for the transitions for $m^* = 2.546$. Thus, to find the equivalent transition for, say, $m^* = 1.0$, that occurs at $U_r = 6$ for $m^* = 2.546$ (initially to mode B at $Re = 261.3$), simulations can be undertaken at $m^* = 1.0$ for $Re = 261.3$ varying U_r to find when $f(D/U) = 0.1729$. For $m^* = 1$, this occurs for $U_r = 6.37$, and indeed determining the Floquet multiplier for this Re–U_r combination for $\lambda/D = 1$ gives $\mu = 1.0$ in agreement with the $m^* = 2.546$ result.

3.8. *Differences in 2-D and 3-D amplitude responses*

In order to show the differences between 3-D and 2-D VIV simulations, even at relatively low Reynolds numbers, direct 3-D numerical simulations were undertaken. Figure 20 illustrates the comparison between 2-D and 3-D simulations at $Re = 300$ for $m^* = 2.546$. This particular Reynolds number choice is interesting because the previous transition analysis shows that the wake should be 3-D except for the highest-amplitude cases. Indeed, the predicted maximum amplitudes for the 3-D simulations centred in the neighbourhood of $U_r = 4$ agree for predictions from 2-D simulations. A check on these cases does indicate that the wake remains 2-D there. However, there are significant differences between the amplitude response at smaller and larger reduced velocities. In particular, the predicted 3-D amplitudes between $4.5 \lesssim U_r \lesssim 8$ are significantly larger than their 2-D counterparts and the response branch is beginning to show the typical response observed in high-Reynolds-number experiments (where the lower branch maintains an almost constant amplitude until finally dropping at higher reduced velocity after desynchronisation (e.g.
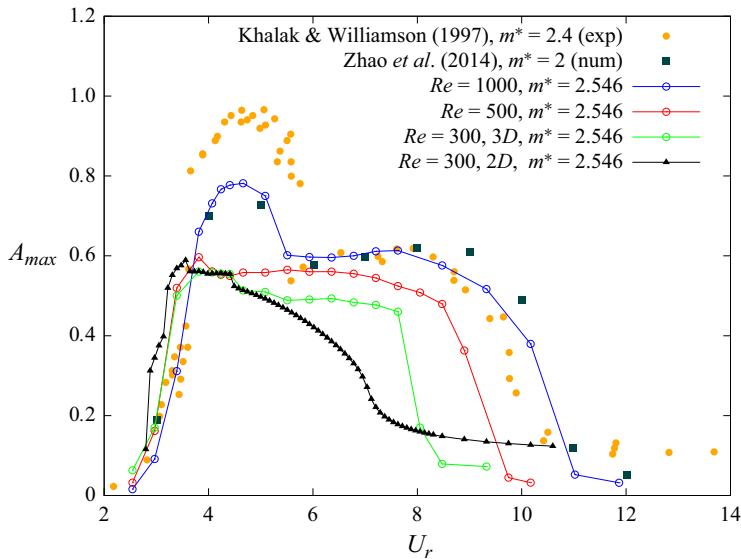
984 A12-30

Figure 21. Amplitude response for 2-D and 3-D simulations with respect to U_r at $Re = 300$ for $m^* = 2.546$.

Khalak & Williamson 1997). Although less noticeable, the initial branch amplitude is also over-predicted in the 2-D simulation. Both the 2-D and 3-D simulations fail to predict the upper branch, where the response amplitude is largest.

3.9. *Amplitude response as the wake becomes increasingly turbulent*

We also used 3-D simulations to examine the response curves as the flow becomes increasingly turbulent, especially to document the appearance of the upper branch and to further determine differences from 2-D simulation predictions. The response curves are shown in figure 21 for $Re = 300$, 500 and 1000. These predictions are compared with the experimental response curve for $m^* = 2.4$ of Khalak & Williamson (1997) for $2000 < Re < 12\,000$, and numerical simulation results from Zhao *et al.* (2014) at a slightly smaller mass ratio of 2. There is excellent agreement between the current predictions and those of Zhao *et al.* (2014), noting the effect of the smaller mass ratio is to extend the reduced velocity range of the lower branch slightly. Both sets of simulations predict a noticeable upper branch. The amplitude in the upper branch is below that seen in experiments, which is consistent with the previous observed dependence of the upper branch amplitude with Reynolds number for VIV (Govardhan & Williamson 2006; Rajamuni *et al.* 2018). On reducing the Reynolds number to $Re = 500$, the upper branch disappears. This was also observed by Blackburn *et al.* (2001) for simulations for $Re = O(500)$. That study focused on demonstrating that shedding in the lower branch was of type $2P$, consistent with experiments unlike the typical $2S$ wake seen over most of the resonant range in lower-Re simulations.

In terms of the lower branch wake state observed in the current set of simulations, figure 22 provides a comparison of wake vortices at $Re = 300$ for the 2-D (*a*) and 3-D (*b*) simulations for $U_r = 7.5$. Thus, development of 3-D flow changes the wake from $2S$ (for 2-D) to $P + S$ (for 3-D), which can be associated with the higher lower-branch response amplitude in the latter case. On increasing the Reynolds number to $Re = 500$, the lower-branch wake changes to a $2P$ mode, as shown in figure 23 and consistent with
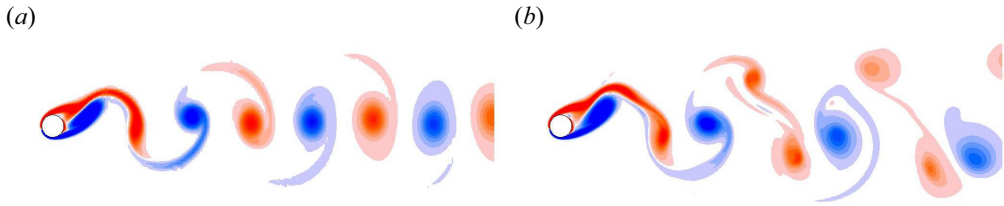
(*a*)　　　　　　　　　　　　　　　　　　　(*b*)

Figure 22. Effect of 3-D transition on the lower branch. (*a*) Spanwise vorticity contours at $Re = 300$, $m^* = 2.546$, $U_r = 7.5$ for 2-D flow. (*b*) Same for 3-D flow at a representative spanwise cross-section.

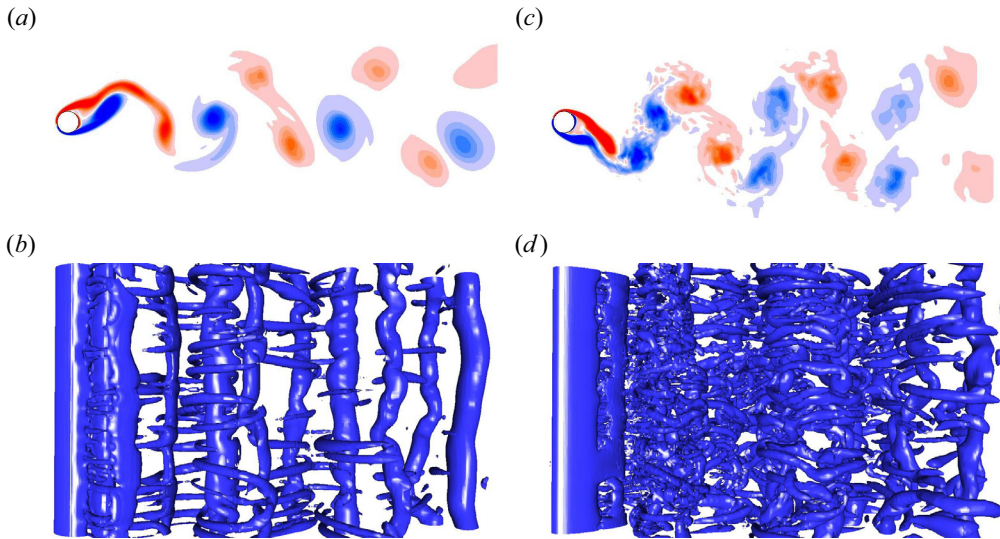(*a*)　　　　　　　　　　　　　　　　　　　(*c*)

(*b*)　　　　　　　　　　　　　　　　　　　(*d*)

Figure 23. Mode selection for the lower branch as Reynolds number is increased. (*a*) Span-averaged spanwise vorticity contours at $m^* = 2.546$, $U_r = 7.5$ and $Re = 300$ for 3-D flow. (*b*) $P + S$ wake mode for this case depicted using isosurfaces of Q-criterion ($Q = 0.1$). (*c*) Same as (*a*) for $Re = 500$, showing the mode has switched to $2P$. (*d*) Corresponding Q-criterion contours for this case.

Blackburn *et al.* (2001). The top two images display spanwise-averaged wake vorticity contours for $Re = 300$ (left) and $Re = 500$ (right). The bottom row of images shows a top down view of these wakes visualised using isosurfaces of constant Q-criterion ($Q = 0.1$), which highlights rotational vorticity rather than shear. Clearly, the $Re = 300$ wake is much less complex, although there is still significant distortion of the spanwise rollers. At $Re = 500$, the wake is effectively turbulent while still showing the remnants of the instability modes examined in this paper.

4. Conclusions

FSA of flow past a circular cylinder undergoing VIV subject to standard elastic support has been undertaken. It has been found that for $Re = 300$, all three previously identified stationary cylinder wake modes, A, B and QP, can be observed. In this case, 3-D transition is through mode B for a spanwise wavelength of $\lambda \approx 0.9D$, close to the value observed for a stationary cylinder, whereas modes A have Floquet multipliers less than unity and so remain stable at this transition Re. Over the resonant reduced-velocity range $U_r \in [4.5, 8]$ corresponding to purely periodic shedding, the 3-D onset mode changes from mode B

984 A12-32

to mode A via mode QP as U_r is increased. Interestingly, for $U_r = 4.5$, a subharmonic (SH) mode is observed and is found to be the critical mode. In all other cases, mode A is observed instead of mode SH. This may be due to the higher amplitude and lower frequency of oscillation as compared to the other reduced-velocity cases examined. The critical *Re* for 3-D transition has been observed to decrease as U_r increases from 4.5 to 8, with the critical mode changing from mode B to mode A.

Thus, each of the modes A, B, QP and SH have been shown to drive the wake transition from 2-D to 3-D flow depending on the amplitude of oscillation and reduced velocity considered. The maximum *Re* for which the wake is guaranteed to remain 2-D for reduced velocities covering the resonant response range, $U_r \in [4.5, 8.0]$, is 202. The 3-D simulations at $Re = 300$ show that the amplitude response curve is distinctly different from that obtained using 2-D simulations. This study improves our understanding of 3-D wake transition for a circular cylinder undergoing VIV under standard elastic mounting, documenting how response oscillation amplitude and reduced velocity effect transition.

Declaration of interests. The authors report no conflict of interest.

Author ORCIDs.
- Rahul Mishra https://orcid.org/0000-0003-2674-2398;
- Rajneesh Bhardwaj https://orcid.org/0000-0003-2995-7394;
- Mark C. Thompson https://orcid.org/0000-0003-3473-2325.

REFERENCES

BAO, Y., HUANG, C., ZHOU, D., TU, J. & HAN, Z. 2012 Two-degree-of-freedom flow-induced vibrations on isolated and tandem cylinders with varying natural frequency ratios. *J. Fluids Struct.* **35**, 50–75.

BARKLEY, D. & HENDERSON, R.D. 1996 Three-dimensional Floquet stability analysis of the wake of a circular cylinder. *J. Fluid Mech.* **322**, 215–241.

BARKLEY, D., TUCKERMAN, L.S. & GOLUBITSKY, M. 2000 Bifurcation theory for three-dimensional flow in the wake of a circular cylinder. *Phys. Rev.* E **61** (5), 5247.

BEARMAN, P.W. 1984 Vortex shedding from oscillating bluff bodies. *Annu. Rev. Fluid Mech.* **16** (1), 195–222.

BEARMAN, P.W. 2011 Circular cylinder wakes and vortex-induced vibrations. *J. Fluids Struct.* **27** (5–6), 648–658.

BLACKBURN, H.M., GOVARDHAN, R.N. & WILLIAMSON, C.H.K. 2001 A complementary numerical and physical investigation of vortex-induced vibration. *J. Fluids Struct.* **15** (3–4), 481–488.

BLACKBURN, H.M. & LOPEZ, J.M. 2003 On three-dimensional quasiperiodic Floquet instabilities of two-dimensional bluff body wakes. *Phys. Fluids* **15** (8), L57–L60.

BLACKBURN, H.M., MARQUES, F. & LOPEZ, J.M. 2005 Symmetry breaking of two-dimensional time-periodic wakes. *J. Fluid Mech.* **522**, 395–411.

DUSEK, J., GAL, P.L. & FRAUNIE, P. 1994 A numerical and theoretical study of the first Hopf bifurcation in a cylinder wake. *J. Fluid Mech.* **264**, 59–80.

GIORIA, R.S., JABARDO, P.J.S., CARMO, B.S. & MENEGHINI, J.R. 2009 Floquet stability analysis of the flow around an oscillating cylinder. *J. Fluids Struct.* **25** (4), 676–686.

GOVARDHAN, R. & WILLIAMSON, C.H.K. 2000 Modes of vortex formation and frequency response of a freely vibrating cylinder. *J. Fluid Mech.* **420**, 85–130.

GOVARDHAN, R.N. & WILLIAMSON, C.H.K. 2006 Defining the 'modified Griffin plot' in vortex-induced vibration: revealing the effect of Reynolds number using controlled damping. *J. Fluid Mech.* **561**, 147–180.

GUPTA, S., ZHAO, J., SHARMA, A., AMIT, A., HOURIGAN, K. & THOMPSON, M.C. 2023 Two- and three-dimensional wake transitions of a NACA0012 airfoil. *J. Fluid Mech.* **954**, A26.

HOURIGAN, K., THOMPSON, M.C. & TAN, B.T. 2001 Self-sustained oscillations in flows around long blunt plates. *J. Fluids Struct.* **15** (3–4), 387–398.

JACONO, D.L., LEONTINI, J.S., THOMPSON, M.C. & SHERIDAN, J. 2010 Modification of three-dimensional transition in the wake of a rotationally oscillating cylinder. *J. Fluid Mech.* **643**, 349–362.

JIANG, H. & CHENG, L. 2021 Large-eddy simulation of flow past a circular cylinder for Reynolds numbers 400 to 3900. *Phys. Fluids* **33**, 034119.

KARNIADAKIS, G. & SHERWIN, S. 2013 *Spectral/HP Element Methods for Computational Fluid Dynamics*. Oxford University Press.

KARNIADAKIS, G.E., ISRAELI, M. & ORSZAG, S.A. 1991 High-order splitting methods for the incompressible Navier–Stokes equations. *J. Comput. Phys.* **97** (2), 414–443.

KARNIADAKIS, G.E. & TRIANTAFYLLOU, G.S. 1992 Three-dimensional dynamics and transition to turbulence in the wake of bluff objects. *J. Fluid Mech.* **238**, 1–30.

KHALAK, A. & WILLIAMSON, C.H.K. 1997 Fluid forces and dynamics of a hydroelastic structure with very low mass and damping. *J. Fluids Struct.* **11** (8), 973–982.

KHALAK, A. & WILLIAMSON, C.H.K. 1999 Motions, forces and mode transitions in vortex-induced vibrations at low mass-damping. *J. Fluids Struct.* **13** (7–8), 813–851.

KIRBY, R.M. & SHERWIN, S.J. 2006 Stabilisation of Spectral/HP element methods through spectral vanishing viscosity: application to fluid mechanics modelling. *Comput. Meth. Appl. Mech. Engng* **195**, 3128–3144.

LE GAL, P., NADIM, A. & THOMPSON, M.C. 2001 Hysteresis in the forced Stuart–Landau equation: application to vortex shedding from an oscillating cylinder. *J. Fluids Struct.* **15**, 445–457.

LEONTINI, J.S., JACONO, D.L. & THOMPSON, M.C. 2015 Stability analysis of the elliptic cylinder wake. *J. Fluid Mech.* **763**, 302–321.

LEONTINI, J.S., STEWART, B.E., THOMPSON, M.C. & HOURIGAN, K. 2006*a* Wake state and energy transitions of an oscillating cylinder at low Reynolds number. *Phys. Fluids* **18** (6), 067101.

LEONTINI, J.S., THOMPSON, M.C. & HOURIGAN, K. 2006*b* The beginning of branching behaviour of vortex-induced vibration during two-dimensional flow. *J. Fluids Struct.* **22** (6–7), 857–864.

LEONTINI, J.S., THOMPSON, M.C. & HOURIGAN, K. 2007 Three-dimensional transition in the wake of a transversely oscillating cylinder. *J. Fluid Mech.* **577**, 79–104.

LEWEKE, T. & WILLIAMSON, C.H.K. 1998 Three-dimensional instabilities in wake transition. *Eur. J. Mech.* B*/Fluids* **17** (4), 571–586.

MISHRA, R., BHARDWAJ, R., KULKARNI, S.S. & THOMPSON, M.C. 2021 Vortex-induced vibration of a circular cylinder on a nonlinear viscoelastic support. *J. Fluids Struct.* **100**, 103196.

MISHRA, R., SOTI, A., BHARDWAJ, R., KULKARNI, S.S. & THOMPSON, M.C. 2020 Transverse vortex-induced vibration of a circular cylinder on a viscoelastic support at low Reynolds number. *J. Fluids Struct.* **95**, 102997.

MITTAL, S. & SINGH, S. 2005 Flow-induced vibrations at subcritical *Re*. *J. Fluid Mech.* **534**, 185–194.

PARKINSON, G. 1989 Phenomena and modelling of flow-induced vibrations of bluff bodies. *Prog. Aerosp. Sci.* **26** (2), 169–224.

PARNAUDEAU, P., CARLIER, J., HEITZ, D. & LAMBALLAIS, E. 2008 Experimental and numerical studies of the flow over a circular cylinder at Reynolds number 3900. *Phys. Fluids* **20**, 085101.

RAJAMUNI, M.M., THOMPSON, M.C. & HOURIGAN, K. 2018 Transverse flow-induced vibrations of a sphere. *J. Fluid Mech.* **837**, 931–966.

RAO, A., RADI, A., LEONTINI, J.S., THOMPSON, M.C., SHERIDAN, J. & HOURIGAN, K. 2015 A review of rotating cylinder wake transitions. *J. Fluids Struct.* **53**, 2–14.

ROBICHAUX, J., BALACHANDAR, S. & VANKA, S.P. 1999 Three-dimensional Floquet instability of the wake of square cylinder. *Phys. Fluids* **11** (3), 560–578.

RYAN, K., THOMPSON, M.C. & HOURIGAN, K. 2005 Three-dimensional transition in the wake of bluff elongated cylinders. *J. Fluid Mech.* **538**, 1–29.

SARPKAYA, T. 1979 Vortex-induced oscillations: a selective review. *J. Appl. Mech.* **46** (2), 241–258.

SARPKAYA, T. 2004 A critical review of the intrinsic nature of vortex-induced vibrations. *J. Fluids Struct.* **19** (4), 389–447.

SHARMA, G., GARG, H. & BHARDWAJ, R. 2022 Flow-induced vibrations of elastically-mounted C-and D-section cylinders. *J. Fluids Struct.* **109**, 103501.

SHEARD, G.J., THOMPSON, M.C. & HOURIGAN, K. 2003 From spheres to circular cylinders: the stability and flow structures of bluff ring wakes. *J. Fluid Mech.* **492**, 147–180.

SHEARD, G.J., THOMPSON, M.C. & HOURIGAN, K. 2005 Subharmonic mechanism of the mode C instability. *Phys. Fluids* **17** (11), 111702.

SOTI, A.K., ZHAO, J., THOMPSON, M.C., SHERIDAN, J. & BHARDWAJ, R. 2018 Damping effects on vortex-induced vibration of a circular cylinder and implications for power extraction. *J. Fluids Struct.* **81**, 289–308.

THOMPSON, M.C., HOURIGAN, K., CHEUNG, A. & LEWEKE, T. 2006 Hydrodynamics of a particle impact on a wall. *Appl. Math. Model.* **30** (11), 1356–1369.

THOMPSON, M.C., HOURIGAN, K. & SHERIDAN, J. 1996 Three-dimensional instabilities in the wake of a circular cylinder. *Expl Therm. Fluid Sci.* **12** (2), 190–196.

THOMPSON, M.C., LEWEKE, T. & WILLIAMSON, C.H.K. 2001 The physical mechanism of transition in bluff body wakes. *J. Fluids Struct.* **15**, 607–616.

WILLIAMSON, C.H.K. 1988 The existence of two stages in the transition to three-dimensionality of a cylinder wake. *Phys. Fluids* **31** (11), 3165–3168.

WILLIAMSON, C.H.K. 1996 Vortex dynamics in the cylinder wake. *Annu. Rev. Fluid Mech.* **28** (1), 477–539.

WILLIAMSON, C.H.K. & GOVARDHAN, R. 2004 Vortex-induced vibrations. *Annu. Rev. Fluid Mech.* **36**, 413–455.

WILLIAMSON, C.H.K. & GOVARDHAN, R. 2008 A brief review of recent results in vortex-induced vibrations. *J. Wind Engng Ind. Aerodyn.* **96** (6–7), 713–735.

WU, X., GE, F. & HONG, Y. 2012 A review of recent studies on vortex-induced vibrations of long slender cylinders. *J. Fluids Struct.* **28**, 292–308.

ZHAO, M. 2013 Flow induced vibration of two rigidly coupled circular cylinders in tandem and side-by-side arrangements at a low Reynolds number of 150. *Phys. Fluids* **25** (12), 123601.

ZHAO, M., CHENG, L., AN, H. & LU, L. 2014 Three-dimensional numerical simulation of vortex-induced vibration of an elastically mounted rigid circular cylinder in steady current. *J. Fluids Struct.* **50**, 292–311.